INORGANIC CHEMISTRY
FRONTIERS

REVIEW

View Article Online
View Journal | View Issue

Cite this: *Inorg. Chem. Front.*, 2023, **10**, 3781

Halide perovskite photovoltaic-electrocatalysis for solar fuel generation

Jin Wook Yang,†[a] You Jin Ahn,†[a] Deok Ki Cho,†[a] Jin Young Kim *[a] and Ho Won Jang *[a,b]

Received 18th April 2023,
Accepted 31st May 2023

DOI: 10.1039/d3qi00714f

rsc.li/frontiers-inorganic

Photovoltaic-electrochemical (PV-EC) fuel production is a promising technology that combines solar energy conversion and electrochemical catalysis to produce sustainable hydrogen and hydrocarbon from renewable sources. Halide perovskite solar cells with adjustable band gaps are attractive for PV-EC devices since their tailored photovoltages in tandem structures with other photovoltaic materials can boost electrochemical reactions without an external power supply. Herein, we mainly focus on halide perovskite photovoltaic-electrochemical fuel generation. The principles and design classification of PV-EC devices, as well as the band gap engineering of halide perovskites for solar cells, are presented. We explicate the mechanism of the oxygen evolution reaction, hydrogen evolution reaction, and CO_2 reduction reaction, suggesting adequate material candidates of electrocatalysts for each reaction. Recent advances in electrocatalysts for water splitting and CO_2 conversion, halide perovskite solar cells, and PV-EC devices for improving solar-to-fuel conversion efficiency are summarized. This review presents significant advances in PV-EC fuel production from a materials point of view, providing a groundwork for its component design.

1. Introduction

The production of renewable fuels from abundant sources such as water and carbon dioxide is an essential step towards achieving a sustainable energy future. Photovoltaic-electrochemical (PV-EC) fuel generation is a promising technology that utilizes solar energy to drive the production of hydrogen and hydrocarbon through electrochemical reactions. The process involves using photovoltaic cells to convert solar energy into electrical energy, which is then used to drive the electrochemical reactions for fuel production.[1–3] PV-EC fuel generation has gained significant interest in recent years due to its potential to provide a carbon-neutral source of renewable fuels. Using solar power to drive fuel production offers a sustainable and environmentally friendly alternative to traditional fossil fuel-based approaches.

In recent years, halide perovskites have emerged as a promising class of materials for photovoltaic and electrochemical

[a]*Department of Materials Science and Engineering, Research Institute of Advanced Materials, Seoul National University, Seoul 08826, Republic of Korea. E-mail: jykim.mse@snu.ac.kr, hwjang@snu.ac.kr*
[b]*Advanced Institute of Convergence Technology, Seoul National University, Suwon 16229, Republic of Korea*
† These authors contributed equally.

Jin Wook Yang

Jin Wook Yang received his Ph.D. from the Department of Materials Science and Engineering at Seoul National University in 2023. He is currently working as a postdoc fellow under the supervision of Prof. Ho Won Jang. His research interests include materials synthesis and designing (photo)electrocatalysts for energy conversion devices.

You Jin Ahn

You Jin Ahn is currently a Ph.D. candidate under the supervision of Prof. Jin Young Kim at the Department of Materials Science and Engineering at Seoul National University. She received her B.S. degree whilst in the Department of Materials Science and Engineering at Seoul National University in 2019. Her research interests include perovskite solar cells for solar energy conversion.

applications.[4–7] In particular, their high-power conversion efficiency (PCE) and tunable band gap have made them attractive for use in solar cells. One particularly interesting application of halide perovskites is PV-EC fuel generation since it is possible to provide customized photovoltage for the electrochemical reaction depending on the configuration of the tandem solar cell.[8–10]

This review aims to provide a comprehensive overview of the state-of-the-art halide perovskite photovoltaic-electrochemical fuel generation. First, we introduce fundamental principles and design classification of PV-EC devices. Then, we deal with the mechanisms of halide perovskite solar cells and electrocatalysts, which are key components of PV-EC devices. We introduce the reaction steps of oxygen evolution reaction (OER), hydrogen evolution reaction (HER), and CO_2 reduction reaction (CRR), which constitute water splitting and CO_2 conversion, and present promise materials candidates for each reaction based on density functional theory (DFT) calculations. Additionally, the review will discuss the recent advances in electrocatalysts focused on each reaction, halide perovskite solar cells, and PV-EC devices for improving the solar-to-fuel (STF) conversion efficiency for fuel production. Finally, we will provide an outlook on future research directions and potential opportunities for developing PV-EC fuel generation technology.

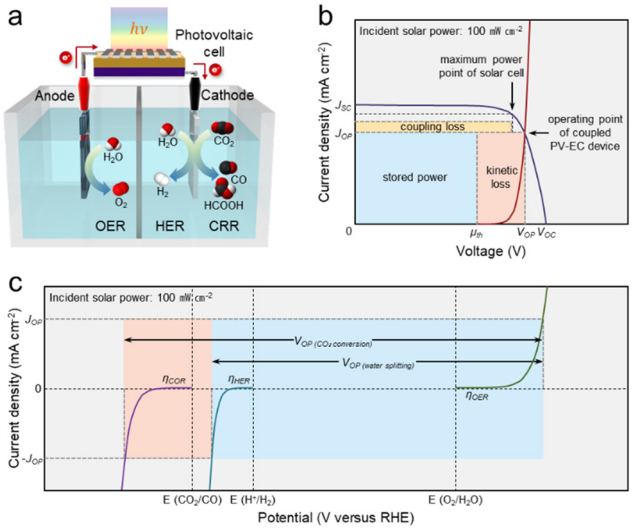

Fig. 1 The principles of photovoltaic-electrochemical (PV-EC) device. (a) Schematic of PV-EC cell. (b) The generalized current density-voltage (*J*–*V*) diagram (2-electrode measurement) of a directly coupled PV-EC device. Reproduced from ref. 13. Copyright 2013 PNAS. (c) The generalized *J*–*V* diagrams (3-electrode measurement) of anode and cathode for electrochemical reactions (water splitting and CO_2 conversion).

2. PV-EC fuel generation

2.1. Principles of PV-EC devices

A PV-EC device consists of electrocatalysts where redox reactions occur and solar cells that generate photovoltage by receiving sunlight. Fig. 1a shows a general PV-EC cell, which is a 2-electrode system comprising an anode for the oxidation reaction and a cathode for the reduction reaction. This review deals with representative solar fuel generation reactions, water splitting, and CO_2 conversion. For these reactions, the following OER by the water oxidation occurs at the anode to generate protons for fuel (hydrogen, carbon monoxide (CO), and formate ($HCCO^-$)) generation.[11]

$$\mathrm{OER}: 2H_2O + 4h^+ \rightarrow O_2 + 4H^+, \quad E^\circ_{ox} = 1.23\ V_{NHE}$$

At the cathode, protons that have received electrons are reduced, inducing HER or CRR according to the following equations.

$$\mathrm{HER}: 2H^+ + 2e^- \rightarrow H_2, \quad E^\circ_{red} = 0.00\,V_{NHE}$$

Deok Ki Cho

Deok Ki Cho is currently a Ph.D. candidate under the supervision of Prof. Jin Young Kim at the Department of Materials Science and Engineering at Seoul National University. He received his B.S. degree in Materials Science and Engineering from Seoul National University of Science and Technology in 2018. His research interests include materials synthesis and designing electrocatalysts for energy conversion.

Jin Young Kim

Jin Young Kim is an associate professor of the department of materials science and engineering in Seoul National University. He received his Ph.D. from the department of materials science and engineering in Seoul National University in 2006. He worked as a postdoctoral researcher and research staff at the National Renewable Energy Laboratory (NREL) from 2007 to 2011. Before he joined Seoul National University in 2015, he worked at the Korea Institute of Science and Technology (KIST) as a senior research scientist. His research interests include inorganic and inorganic/organic hybrid materials for solar energy conversion.

$$\mathrm{CRR(CO)}: \mathrm{CO_2} + 2\mathrm{H^+} + 2\mathrm{e^-} \rightarrow \mathrm{CO} + \mathrm{H_2O},$$
$$E^{\circ}_{\mathrm{red}} = -0.11\,\mathrm{V_{NHE}}$$

$$\mathrm{CRR(HCOO^-)}: \mathrm{CO_2} + 2\mathrm{H^+} + 2\mathrm{e^-} \rightarrow \mathrm{HCOO^-} + H^+,$$
$$E^{\circ}_{\mathrm{red}} = -0.31\,\mathrm{V_{NHE}}$$

To proceed with actual reactions, overpotentials to overcome the kinetic barriers are required in addition to the thermodynamic redox potential differences. Therefore, in the PV-EC device, the photovoltage of the solar cell and the electrolyzer's cell voltage, including the overpotential, should be matched without external bias. As shown in the generalized current density–voltage (J–V) diagram of a PV-EC device measured in a 2-electrode system (Fig. 1b), the operating voltage (V_{OP}) is determined at the intersection of the curves for the PV cell and the electrolyzer. At the operating point, the STF conversion efficiency (η_{STF}) is calculated as below:

$$\eta_{\mathrm{STF}} = \frac{J_{\mathrm{OP}}[\mathrm{mA\,cm^{-2}}] \times \Delta E^0[V] \times \eta_{\mathrm{F}}}{P_{\mathrm{s}}[\mathrm{mW\,cm^{-2}}]},$$

where J_{OP} is the operating current density (J_{OP}), ΔE^0 is the thermodynamic potential difference between redox reactions, η_{F} is the faradaic efficiency, and P_{s} is the solar power density.[12] The solar-to-hydrogen (STH) conversion efficiency (η_{STH}) in water splitting system requiring a voltage of 1.23 V is expressed as below:

$$\eta_{\mathrm{STH}} = \frac{J_{\mathrm{OP}}[\mathrm{mA\,cm^{-2}}] \times 1.23V \times \eta_{\mathrm{F}}}{P_{\mathrm{s}}[\mathrm{mW\,cm^{-2}}]}.$$

The product of thermodynamic reaction potential (μ_{th}) and J_{OP} is stored as fuel production power.[13] And the product of the overpotential (difference between V_{OP} and μ_{th}) and J_{OP} is the kinetic loss derived from reaction kinetic barriers. Also, coupling loss is defined as the difference between the maximum output of the solar cell and the power dissipated in the electrolyzer. The characteristics of components in the electrolyzer are evaluated by the polarization curves of a 3-electrode system composed of working, counter, and reference electrodes. Fig. 1c shows the generalized J–V diagrams of the anode and cathode in the 3-electrode system. Generally, an overpotential is defined as the additional bias required to generate a current density of 10 mA cm^{-2} in each reaction. Also, for PV-EC devices, the potential differences at which the OER of the anode and the HER of the cathode generate J_{OP} correspond to the V_{OP} of the overall water splitting. This is consistent with the J–V curves in Fig. 1b and also applies to the overall CO_2 conversion configured with OER and CRR.

In summary, several parameters can significantly impact the STF conversion efficiency of photovoltaic-electrocatalysis. The PCE of the solar cell directly affects the amount of electricity generated from solar energy. Higher PCE values result in increased energy availability for fuel production. Also, minimizing the overpotential of electrocatalysts is crucial for improving overall efficiency by reducing energy losses. Comprehensively, it is crucial that the photocurrent generated by the PV cell matches the electrocatalytic current requirements.

2.2. Design classification of PV-EC devices

PV-EC devices are classified into three types according to the position of the PV cell and the coupling configuration between the solar cell and electrodes.[14] Fig. 2 illustrates the design classification of different PV-EC devices, including open and flow cells. For type I, the PV cell is combined with the catalyst electrodes on both sides and completely immersed in the elec-

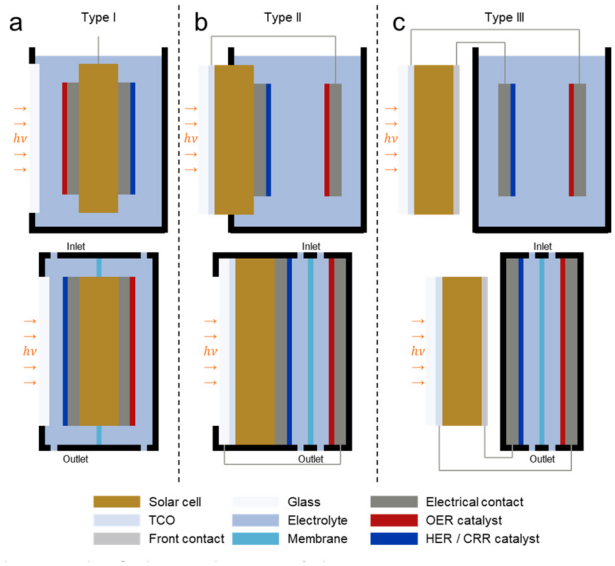

Fig. 2 Design classification of different PV-EC devices including both open cell and flow cell. For type I (a), the PV cell is completely immersed in the electrolyte with the catalyst electrodes on both sides. For type II (b), only one side of the PV cell is exposed to the electrolyte. For type III (c), PV and EC elements are separated. Reproduced from ref. 14. Copyright 2016 Nature Publishing Group.

Ho Won Jang

Ho Won Jang is a full professor at the Department of Materials Science and Engineering in Seoul National University. He received his Ph.D. from the Department of Materials Science and Engineering at Pohang University of Science and Technology in 2004. He worked as a research associate at the University of Madison-Wisconsin from 2006 to 2009. Before he joined Seoul National University in 2012, he worked at the Korea Institute of Science and Technology (KIST) as a senior research scientist. His research interests include materials synthesis and device fabrication for (photo)electrocatalysis, chemical sensors, memristors, micro-LEDs, and thin film transistors.

trolyte (Fig. 2a). It is similar to the photocatalyst in that there are no external wires and properties are evaluated by production yield. This type must be accompanied by the perfect capping of the solar cell and transparent catalyst layer and has been reported in various research.[15,16] Reece *et al.* fabricated a wireless type I PV-EC cell by attaching a Co-based OER catalyst and NiMoZn HER catalyst to a triple junction Si solar cell.[17] For type II, one side of the PV cell is covered with the catalyst and exposed to the electrolyte (Fig. 2b). This structure is similar to the form of a photoelectrode in which solar cell materials are used as the light absorber by coating cocatalyst layers.[18–20] It has the advantage of independently optimizing the optical and electrochemical properties while simplifying the entire system by monolithic structures.[21,22] Appleby *et al.* implemented a type II PV-EC cell by coating the RuO_2 catalyst on the surface of the Si tandem solar cell.[21] Finally, for type III, the solar cell is connected to both anode and cathode with external wires and is located outside the electrolyte (Fig. 2c). Although this type is structurally complicated, it has the advantage of freely arranging solar cells. Especially, it is advantageous for PV-EC systems using halide perovskite-based solar cells that are vulnerable to moisture. Most PV-EC systems correspond to type III with electrical wires.[23–25] Luo *et al.* designed an open PV-EC cell by combining a perovskite/Si tandem solar cell with bifunctional NiFe catalyst electrodes. The type III water splitting generated a STH conversion efficiency of 12.3%.[26] Also, Cheng *et al.* reported a solar-driven CO_2 conversion flow cell directly powered by GaInP/GaInAs/Ge triple-junction solar cell. The type III PV-EC cell recorded a high STF conversion efficiency of 19.1%.[27]

2.3. Halide perovskite photovoltaics

Solar cells that produce photovoltage *via* sunlight work as a voltage supplier in the PV-EC device. The overall water splitting of a general electrolyzer consisting of the anode and cathode is driven electrically, but the PV-EC devices are distinguished from it as a type of solar water splitting. Many PV-EC studies have been conducted using various photovoltaic cells such as Si,[28,29] GaAs,[30,31] CZTSSe,[32,33] GIGS,[34,35] organic,[36,37] and dye-sensitized solar cells.[38,39] This review covers halide perovskite solar cell-based PV-EC devices as the main content. Perovskite is a generic term for minerals that have the crystal structure of $CaTiO_3$, which was first discovered in 1839. Among them, halide perovskites are a class of materials that have received much attention in recent years for their potential applications in photovoltaic cells, light-emitting devices, and other optoelectronic devices. As illustrated in Fig. 3a, the halide perovskites have a general formula AMX_3, where A is monovalent or non-coordinating cations (Cs, methylammonium (MA), formamidinium (FA)), M is a bivalent p-block metal (Pb, Sn), and X is halogens (I, Br, Cl).

Halide perovskites have shown promise for use in solar cells, light-emitting diodes, and other optoelectronic applications due to their high efficiency and low-cost production.[40,41] Especially, halide perovskites have unique properties that make them attractive for solar cells, including a high absorption coefficient, long charge carrier diffusion length, and tunable band gap. Indeed, the band gap of halide perovskites can be tuned from 1 to 5 eV depending on the constituent ions and composition, enabling light harvesting from UV to near IR spectral range.[8,42] When halide perovskites become a solid state, molecular orbitals form the valence band (VB) and conduction band (CB), and their band gaps are controlled as the density of state varies greatly depending on the constituent ions.[4] As shown in Fig. 3b, Castelli *et al.* calculated 240 band gaps of halide perovskites composed of Cs, MA, and FA as A-cation, Sn and Pb as M-ion, and a combination of Cl, Br, and I as X anions.[43] Here, it can be seen that the band gap varies according to cation, anion, and phase, and the band gap generally tends to increase in the direction of the red arrow.

When the halide perovskite with various band gaps is used as the light absorber, the photovoltage and photocurrent density of the solar cell can be easily controlled. As the band gap increases, the photovoltage increases, but the photocurrent density decreases because of the reduction of absorption spectra. This appears as a trade-off between photovoltage

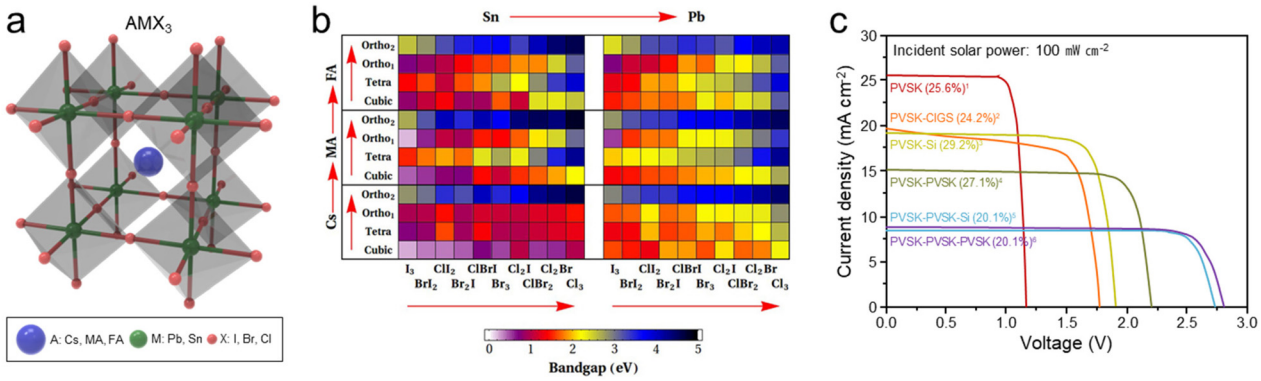

Fig. 3 Halide perovskite-based solar cells. (a) General crystal structure (AMX_3) of the halide perovskite. (b) Calculated band gaps of halide perovskites with different composition and phase. Reproduced from ref. 43. Copyright 2014 AIP Publishing. (c) *J*–*V* curves of various halide perovskite tandem solar cells with benchmarked power conversion efficiencies (PCE). Benchmark list: (1) ref. 55, (2) ref. 46, (3) ref. 54, (4) ref. 53, (5) ref. 52, (6) ref. 56

and photocurrent density within the fixed power of the solar cell. To solve this trade-off and increase the PCE of the solar cell, the tandem solar cell composed of two or more light absorbers has been proposed. Short wavelength light is absorbed by the large band gap material, and transmitted long wavelength light is absorbed by the small band gap material. Halide perovskites also compose tandem solar cells with other photovoltaic materials such as Si (1.12 eV),[44,45] CIGS (1.01–1.68 eV),[46,47] CZTS (1.0–1.4 eV),[48,49] and organic materials.[50,51] In Fig. 3c, *J*–*V* curves of various halide perovskite tandem solar cells with benchmarked power conversion efficiencies were compared.[46,52–56] Through more sophisticated band gap control of subcell materials and multilayer interface engineering, the PCE for each type of halide perovskite tandem solar cell has been continuously increased. As the number of subcells constituting the tandem solar cell increases, the open circuit voltage (V_{oc}) increases, and the short circuit current density (J_{sc}) decreases since the photovoltage is merged and the current density converges to the lower value. In order to produce high STF conversion efficiencies while meeting the required voltages (thermodynamic potential differences + overpotentials) for the overall water splitting or CO_2 conversion, solar cells with V_{oc} and J_{sc} suitable for each reaction should be customized. More details are covered in chapter 3.

2.4. Electrocatalysis

Prior to the design of the electrocatalyst, a key component of the PV-EC system, it is necessary to understand the reaction mechanism by the DFT calculation since the number of involved electrons and reaction steps is different for each electrochemical reaction. OER at the anode is a 4-electron transfer reaction comprising the following 4 sub-steps in alkaline media:

$$* + OH^-(aq) \rightarrow *OH + e^- \quad \Delta G_1$$

$$*OH + OH^-(aq) \rightarrow *O + e^- + H_2O \quad \Delta G_2$$

$$*O + OH^-(aq) \rightarrow *OOH + e^- \quad \Delta G_3$$

$$*OOH + OH^-(aq) \rightarrow O_2\ (g) + e^- + H_2O + * \quad \Delta G_4$$

Since the Gibbs free energy difference between the second and third sub-step ($\Delta G_{OH^*} - \Delta G_{OOH^*}$) is generally 3.2 eV, $\Delta G_{OH^*} - \Delta G_{O^*}$ as an OER descriptor determines the rate-determining step for OER according to its value.[57] Fig. 4a indicates a volcano plot in which the OER overpotential as a function of the descriptor has a vertex.[58] Based on DFT calculations, various metal oxides are plotted along with the lines, and among them, Co_3O_4 and RuO_2 show the highest OER activity. Since the OER, 4 electron–proton coupling reaction, has very sluggish kinetics, the oxygen evolution electrocatalyst with high activity is essential to reduce the overall overpotential of the electrolyzer. As the engineering for the OER catalyst, various materials such as oxide,[59,60] hydroxide,[61,62] sulfide,[63,64] and phosphide[65,66] based on multi-component metal alloys have been studied. Also, research has recently attempted to introduce single-atom catalysts on the existing catalyst materials.[67–69] Atomically dispersed catalysts are

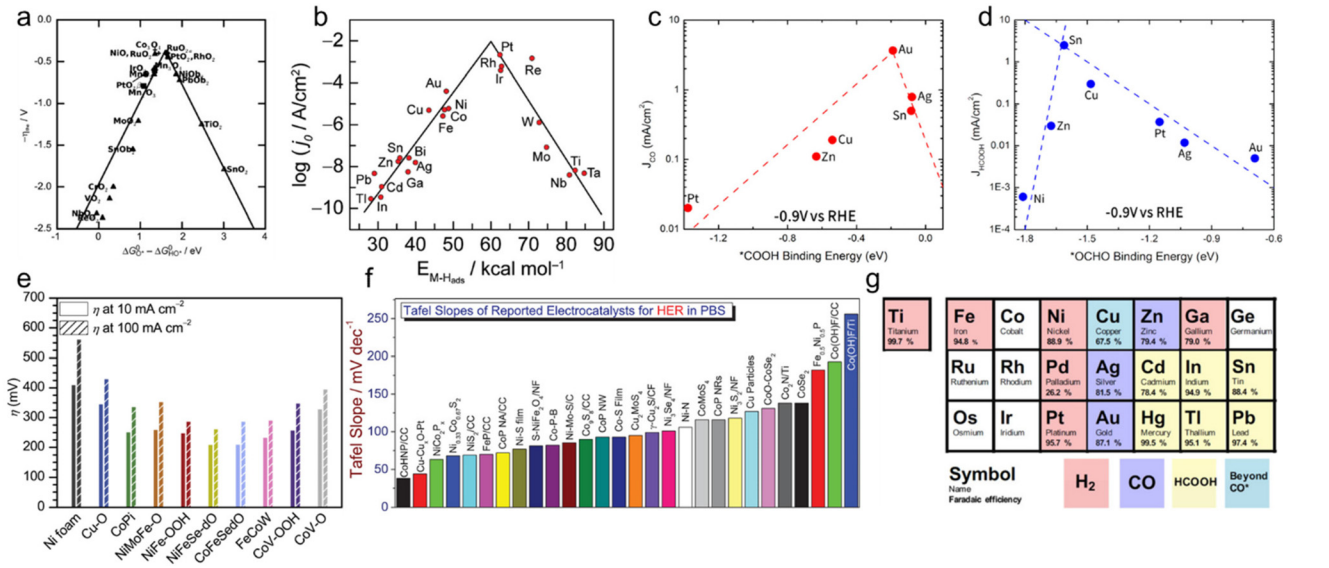

Fig. 4 Volcano plots and catalytic activity of electrocatalysts for different electrochemical reactions. (a) Volcano plot for the oxygen evolution reaction (OER) as a function of the standard free energy. Reproduced from ref. 58. Copyright 2011 Wiley. (b) Volcano plot for the hydrogen evolution reaction (HER) as a function of M-H bonding energy. Reproduced from ref. 71. Copyright 2010 American Chemical Society. Volcano plots for the CO_2 reduction reaction (CRR) to (c) CO using *COOH binding energy and (d) $HCOO^-$ using *OCHO binding energy. Reproduced from ref. 78. Copyright 2017 American Chemical Society. (e) Overpotentials of OER catalysts on Ni foam (NF) in 1 M KOH. Reproduced from ref. 70. Copyright 2021 Cell Press. (f) Tafel slopes of HER catalysts in PBS solution. Reproduced from ref. 72. Copyright 2020 Wiley. (g) Major product classification of metal catalysts for CRR from experiments by Hori. Reproduced from ref. 80. Copyright 2017 Wiley.

characterized by high catalytic activity while reducing the amount of noble metals. In addition, in order to overpotential by increasing the specific surface area, various catalysts were formed on porous supports such as Ni foam (NF), carbon paper (CP), carbon cloth (CC), and Carbon nanotube (CNT), as shown in Fig. 4e.[70]

HER at the cathode is a 2-electron transfer reaction, consisting of the following 2 sub-steps involving a hydrogen intermediate in acidic media:

$$* + H^+ (aq) + e^- \rightarrow *H \quad \Delta G_1$$

$$*H + H^+ (aq) + e^- \rightarrow H_2 (g) + * \quad \Delta G_2$$

Since HER activity is related to the adsorbed hydrogen intermediate (H*), the Gibbs free energy of hydrogen adsorption (ΔG_{H^*}) becomes HER descriptor in acidic media. Therefore, an ideal catalyst should bind to the reactant at an intermediate strength that is neither too weak nor too strong. In other words, a volcano plot with a maximum point of current density is also drawn according to hydrogen binding energy (ΔG_{H^*}) in HER, as shown in Fig. 4b.[71] Catalytic elements with high HER activity are mostly rare earth metals such as Pt, Rh, Ir, and Re. Therefore, in order to lower the unit cost of the overall water splitting electrolyzer, the cost-effectiveness of the HER catalyst materials is required. Transition metal-based multi-component alloy catalysts and single-atom catalysts through atomic layer deposition (ALD) and electrodeposition have been studied, as shown in Fig. 4f.[72–75]

Unlike water splitting, the CRR, additionally including CO_2 molecules, has various pathways to reach the product. Even in the simplest CRR, in which 2 electrons are involved to produce C^1 products, a CO_2 molecule is divided into two product pathways according to the atomic bonding. The following equations express a representative CRR for generating CO:

$$* + CO_2 (g) + H^+ (aq) + e^- \rightarrow *COOH \quad \Delta G_1$$

$$*COOH + H^+ (aq) + e^- \rightarrow *CO + H_2O \quad \Delta G_2$$

$$*CO \rightarrow CO (g) + * \quad \Delta G_3$$

When carbon atoms bind on the electrode surface in the initial electrochemical step, CO is evolved by forming a *COOH intermediate.[76] The second pathway is the process of generating $HCOO^-$ through the following equations:

$$* + CO_2 (g) + H^+ (aq) + e^- \rightarrow *OCHO \quad \Delta G_1$$

$$*OCHO + H^+ (aq) + e^- \rightarrow *HCOO^- \quad \Delta G_2$$

$$*HCOO^- \rightarrow HCOO^- + * \quad \Delta G_3$$

The *OCHO intermediate is produced when oxygen atoms bind to the electrode surface, concerning the $HCOO^-$ generation.[77] As with HER, the Sabatier principle, where the binding to key intermediates that is neither too strong nor too weak leads to maximum activity, is also applied to CRR. That is, *COOH and *OCHO binding energies are the main descriptors expressing CO and HCOO- production activity, respectively.[78] Fig. 4c shows a volcano plot of CO partial current density at −0.9 V_{RHE} *versus* *COOH binding energy as a descriptor. Au was calculated to have moderate *COOH binding energy and high activity for CO production. Similarly, for the formate production, the partial current density of $HCOO^-$ showed a volcano plot for the *OCHO binding energy as a descriptor, as shown in Fig. 4d. Sn near the top of the volcano plot has an optimal binding energy of the key intermediate *OCHO, showing high selectivity toward $HCOO^-$.

The prediction of the elemental candidate through these DFT calculations of the CO_2 reduction reaction well corresponds to the experimental results. In 1989, Hori *et al.* experimentally proved the faradaic efficiency of metal elements for H_2, CO, HCOOH, and C^2 products produced in the electroreduction process of CO_2.[79] Based on Hori's experiment, Bagger *et al.* classified the elements advantageous to each product and summarized them in a periodic table, as shown in Fig. 4g.[80] As in volcano plots, Au and Sn showed high selectivity for CO and $HCOO^-$ production, respectively. Based on Hori's table, various CRR studies have been conducted with elemental combinations.

3. Advances in halide perovskite solar cells

3.1. Halide perovskite solar cells

Halide perovskite solar cells (PSCs) have emerged as next-generation solar cells owing to their outstanding optoelectronic properties,[81] bandgap tunability,[82–84] and scalable manufacturing capability.[85,86] The PCE of metal halide PSCs has abruptly increased from 3.8% to 25.7% in the past decade.[55,87,88] Wide-bandgap (WBG) single junction PSCs with a V_{oc} of over 1.3 V applicable to a PV-EC system have also been recently reported.[89] To improve the overall efficiency and stability of the PV-EC system and achieve higher efficiency beyond the Shockley–Queisser limits of single junction solar cells,[90] remarkable advances have been made in perovskite-based tandem solar cells (TSCs) such as perovskite/Si, perovskite/perovskite, and perovskite/CIGS.[91] These tandem devices can stably satisfy the operating potential required for the PV-EC system with a high current value.[7] The tandem device consists of two or more complementary subcells that can utilize a wide range of the solar spectrum by effectively mitigating photon loss due to thermalization and transmission in a single-junction device.

The two typical configurations of TSCs are monolithically integrated two-terminal (2-T) and mechanically stacked four-terminal (4-T) configurations, as shown in Fig. 5.[92] The 4-T TSCs structurally require more transparent conducting oxide (TCO) layers than 2-T TSCs, leading to higher parasitic absorption and manufacturing costs. In the 2-T configuration, each subcell is monolithically connected in series through an interconnection layer (ICL). The ICL forms an electrical contact with the adjacent layers for the recombination of electrons and holes from the individual subcells. Thus, ICLs with high

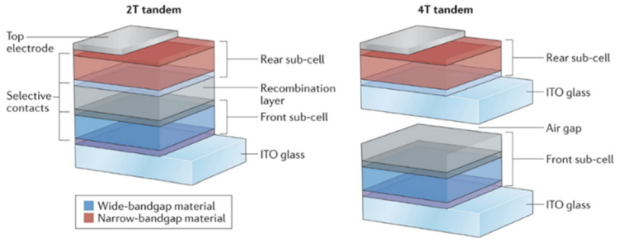

Fig. 5 Diagram of the architecture of two-terminal (2-T) and four-terminal (4-T) tandem solar cells. Reproduced from ref. 92. Copyright 2017 Nature Publishing Group.

optical transparency and conductivity are required to obtain high-performance tandem devices.[93] Particularly in all-perovskite TSCs, ICL should also act as a protection layer to prevent the deterioration of the pre-deposited subcell from the solution process of subsequent perovskite layer fabrication.[94] Because two or more cells in 2-T tandem devices are connected in series, the J_{sc} of the tandem devices is limited by the lower one. The precise matching of J_{sc} by controlling the thickness and bandgap of perovskite films is important to improve the overall current of the tandem devices. The ideal top cell bandgap of the perovskite/Si TSC is constrained to a narrow range of 1.7–1.8 eV, and the ideal bandgap combination of the all-perovskite TSC is 1.2–1.25 eV for the narrow-band gap (NBG) subcell and 1.7–1.8 eV for the WBG subcell.[5] Despite the complexity and difficulty of the fabrication process, perovskite-based 2-T tandem devices have been actively studied due to their enormous potential and cost-effectiveness.[95–97] Therefore, here, we cover the recent progress and challenges of the 2-T monolithic perovskite/Si and all-perovskite TSCs, which are rapidly obtaining notable achievements.

3.2. Perovskite/Si tandem solar cells

Perovskite/Si TSCs receive huge attention to realize industrial applications first due to the crystalline silicon (c-Si) solar cells technology market share of more than 95% and their mature scale production.[45,98] Perovskite/Si tandem technology has reached over 31% PCE with the rapid progress in PSCs.[91] The monolithic tandem Perovskite/Si TSC includes a front-side-polished, rear-side-textured, and double-side-textured c-Si as a bottom cell.[99] The c-Si has an indirect bandgap, so they show weak light absorption near their absorption edge. To minimize the light reflection and harvest the maximum amount of light, a double-sided texturing silicon wafer has been employed in a bottom cell of the Perovskite/Si TSC. Werner *et al.* have demonstrated increased light trapping of an infrared region in a bottom cell by texturing the rear side of the silicon wafer.[100] The first fully textured Perovskite/Si tandem cells conformally deposited the WBG perovskite on the micrometer-sized pyramids of textured monocrystalline silicon by a combination of evaporation and solution coating.[101] Using single-step solution-based blade-coating or spin-coating methods, a fully-textured Perovskite/Si tandem device with comparable anti-reflection properties was also fabricated.[102] They deposited WBG perovskite top cells on the front surface of silicon has a texture of less than 2 μm, and achieved certified PCE of 25.7% and stabilized PCE of 26.1%, respectively. However, it is still technically hard to fabricate the WBG perovskite subcell on textured silicon surfaces applying the solution process. The WBG top cell needs to satisfy the thickness over 1 μm to avoid shunting and offer manufacturing capability. At the same time, high-quality WBG perovskite film with long carrier diffusion lengths and reduced non-radiative recombination is required to facilitate charge extraction for efficient tandem devices on fully-textured c-Si. Furthermore, to broaden the bandgap of perovskite to the optimum value for Perovskite/Si TSCs, it is needed to increase the Br content in the perovskite film.[103] However, a high ratio of Br causes light-induced halide segregation and adversely affects the V_{oc} deficits and film degradation under illumination.[104] Yang *et al.* identified that positive iodide interstitials (I_i^+), generated by the small bromide incorporation, act as the dominant deep charge-trapping defects in WBG perovskites.[105] They added trimethylphenylammonium tribromide ($TPABr_3$) into the WBG perovskites to reduce the I_i^+ concentration. Br^{3-} from $TPABr_3$ can occupy halide vacancies and leave two terminal bromine atoms, which can hinder the formation of iodide vacancies and thus reduce the I_i^+ concentration. To demonstrate this, they changed the cation and anion of additives to trimethylphenylammonium chloride (TPACl) and tetrabutylammonium tribromide ($TBABr_3$). As a result, the devices with $TBABr_3$ and $TPABr_3$ showed relatively high V_{oc}, concluding that Br_3^- has more relevance to the V_{oc} enhancement. The reduced bulk trap density in $TPABr_3$-WBG perovskite enables ~1 μm thickness PSCs without a decrease of fill factor (FF) and J_{sc}. Besides, The WBG perovskite films with $TPABr_3$ exhibit no obvious photoluminescence peak shifting or splitting under continuous 10 sun illumination after 120 min in ambient air. The best-performing WBG perovskite cell with 0.2 mol% $TPABr_3$ delivers a V_{oc} of 1.23 V, a J_{sc} of 21.2 mA cm^{-2}, and a FF of 83.8%, resulting in a PCE of 21.9%. They fabricated Perovskite/Si TSCs using blade-coating-optimized 1.65 eV WBG perovskites with $TPABr_3$ on double-side-textured silicon bottom cells with a mean texture size of 0.43 μm, as shown in Fig. 6a. The best-performing tandem device showed a PCE of 28.6%, with a V_{oc} of 1.92 V, a J_{sc} of 19 mA cm^{-2}, and a FF of 78.5% (Fig. 6b and c). Luo *et al.* developed an anion-engineered additive strategy to improve the inferior crystal quality of WBG perovskite films on fully-textured silicon.[106] To conformally deposit WBG perovskite films on industrially feasible silicon, a hybrid two-step deposition method consisting of sequential co-evaporation and the spin-coating process is deployed. First, PbI_2 and CsBr were co-evaporated on the pyramid-shaped textured silicon surface to form an inorganic framework. FAI and FABr solution was sequentially spin-coated onto the inorganic framework, followed by the annealing process. Simultaneously adding a MACl and MASCN in the organic salt solution enlarged the grain size and enabled an excellent conformal deposition of WBG perovskites on the textured silicon surface.

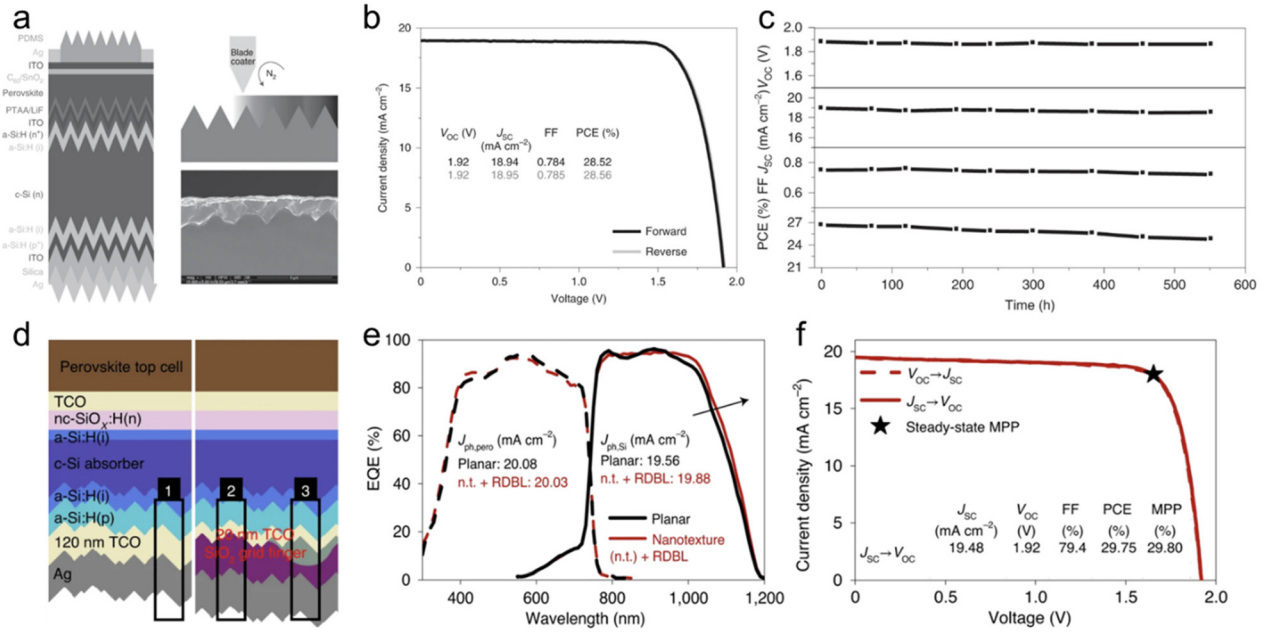

Fig. 6 Perovskite/Si tandem solar cells. (a) Device structures of perovskite/Se tandem cells and with cross-sectional SEM images of blade-coated WBG perovskite films on textured c-Si. (b) *J*–*V* curves of champion monolithic perovskite/Si tandem solar cell. (c) Operational stability of encapsulated tandem device in air at 25 °C. Reproduced from ref. 105. Copyright 2022 Nature Publishing Group. (d) Schematic of the perovskite/Si TSC layer stack with standard reflector with an RDBL at the rear side. The numbered black frames mark the standard rear side (1) and the SiO_2 (2) and grid finger (3) regions of the RDBL. (e) EQE spectra (dashed lines, perovskite EQE; solid lines, silicon EQE) of a planar perovskite/Si TSC with a standard rear side (black) and a nanotextured (n.t.) perovskite/Si TSC with an RDBL (red). The integrated photogenerated current densities of perovskite ($J_{ph,pero}$) and silicon ($J_{ph,Si}$) are shown. (f) *J*–*V* characteristics of a nanotextured perovskite/Si TSC with an RDBL certified by CalLab at Fraunhofer ISE. Reproduced from ref. 107. Copyright 2022 Nature publishing group.

MASCN promoted the crystallization of the α-phase perovskite phase, while MACl retard the whole procedure by forming the intermediate phase until the thermal annealing in the air during the film formation. All photovoltaic parameters were improved for the WBG PSCs, adding both MACl and MASCN, resulting in a PCE of 18.9%. They employed 4-trifluoromethylphenylammonium chloride (CF3-PACl) as a passivator in WBG perovskite with $MA(Cl_{0.5}SCN_{0.5})$ additive. The V_{oc} of the device was dramatically promoted from 1.09 V to 1.19 V, reducing interfacial recombination. The fully textured monolithic Perovskite/Si tandem device with an aperture area of 1.05 cm^2 achieved a champion PCE of 28.9% with a V_{oc} of 1.85 V, a J_{sc} of 19.8 mA cm^{-2}, and a FF of 78.9% and certified PCE of 27.87%. A large area tandem device with an aperture area of 16 cm^2, replacing the spin-coating process with blade-coating to introduce organic salts, reached an efficiency of 25.1% with a V_{oc} of 1.79 V, a J_{sc} of 18.5 mA cm^{-2}, and a FF of 75.7%.

Tockhorn *et al.* present periodic nanotextures on the front surface of the silicon bottom cell that reduce the reflection losses and improve the fabrication yield enabled by the solution-processed film formation.[107] The sinusoidal nanostructure has a hexagonal lattice with a period of 750 nm and a peak-to-valley height of 300 nm, making it possible to the WBG perovskite film to be completely covered by a typical thickness of 500–600 nm on a planar surface. Moreover, the nanotextured silicon surface has improved the ability of perovskite solution to retain compared to planar one, enhancing the process of the yield of WBG PSCs. The nanotexturing surface reduces the reflectance considerably from 3.30 to 2.82 mA cm^{-2} current-density-equivalent and shows statistical improvement of the V_{oc} by around 15 mV compared to the planar surface. A dielectric buffer layer (RDBL) is implemented at the rear side of the silicon bottom cell to reduce parasitic absorption losses in the rear reflector. As a result of the simulation of the photogenerated current density in the silicon with TCO and SiO_2 thickness, RDBL is determined to consist of 20 nm TCO and 180 nm SiO_2 buffer layer, as shown in Fig. 6d (region 2). The external quantum efficiency (EQE) spectra of experimentally realized Perovskite/Si TSCs with and without RDBL feature an increased absorption at the silicon band edge, as shown in Fig. 6e. The best tandem devices with nanostructure interface between Si and perovskite and RDBL reached a PCE of 29.75%, with a V_{oc} of 1.92 V, a J_{sc} of 19.56 mA cm^{-2}, and a FF of 79.4% (Fig. 6f).

Zheng *et al.* reported an ultra-thin 1.7 nm ITO interlayer to provide the interfacing between the silicon and perovskite subcells with minimum parasitic resistance.[108] They found that the J_{sc} remained constant as the ITO thickness varied, while the V_{oc} and especially FF were the highest when the ITO was 1.7 nm thick. Because of the improved lateral conductivity in the ITO layer failing to localize shunting effects, shunt resistance (R_{sh}) decreases with ITO thickness. They also found that

the function of localizing shunts in ultra-thin ITO layers is effective in cells with an area over 1 cm^2, which is less effective in thicker ITO with improved lateral conductivity. The 1.7 nm ultra-thin discontinuous ITO films afford sufficient trap states for the interface between the ITO layer and the a-Si:H layer *via* trap-assisted tunneling. After the application of the anti-reflection layer, a 1 cm^2 tandem device with a V_{oc} of 1.82 V, J_{sc} of 18.1 mA cm^{-2}, and a FF of 82.4% under reverse scan and a steady-state PCE of 27.0% is achieved, which is the highest PCE for an n-i-p based Perovskite/Si TSCs. Large area Perovskite/Si TSCs with 11.8 cm^2 and 65.1 cm^2 cells, including ultra-thin ITO interlayer, were also fabricated and showed PCE of 24.2% and 21.1%, respectively. The stability of an encapsulated tandem cell was tested under 1-sun illumination with MPP tracking, resulting in maintenance of 98% of its initial performance after 600 hours.

To improve the long-term stability of PSCs, research on 2D layered perovskites and inorganic perovskites has also been actively conducted.[109–111] The hydrophobic bulky organic spacer in 2D perovskite enhances the device stability by preventing the decomposition of perovskites and chain reactions that form irreversible PbX_2.[112] Inorganic perovskites with the composition of $CsPbX_3$ have improved thermal and phase stability compared to the perovskites with organic cations.[113] Both perovskites can have bandgaps around 1.7 eV and thus can be applied to the top cell of the perovskite-based tandem device to enhance long-term operational stability. Wang *et al.* introduced a 2-Amino-5-Bromobenzamide (ABA) to passivate the defective top surface of inorganic perovskite films. The carbonyl (C═O) and amino (NH_2) groups of this multifunctional molecule simultaneously coordinate with uncoordinated Pb^{2+}, while Br fills the halide vacancies and inhibits the formation of Pb^0. An ABA-treated inorganic PSC exhibits suppressed interface non-radiative recombination and ion migration, resulting in a high efficiency of 20.38%. Furthermore, the device retains 80.33% of its initial efficiency after 270 h of continuous illumination in ambient air with a relative humidity of 25%. A Si/perovskite TSC with the ABA-treated inorganic perovskite subcell achieved a 25.31% efficiency and maintained 92.59% of initial efficiency after 200 h under continuous illumination in ambient air without encapsulation.[111]

With the rapid progress of perovskite-based double-junction solar cells, a multi-junction solar cell including a perovskite absorption layer is emerging owing to the cost-effectiveness and bandgap-tuning characteristics.[56,114,115] The theoretical efficiency limit for a triple-junction tandem is higher than that of a double-junction, so there is more room for a significant leap in solar cell efficiency.[116] A Si-based multi-junction solar cell is one of the main candidates to achieve the goal. Zheng *et al.* reported a 2-T Perovskite/Perovskite/Si tandem solar cell with a V_{oc} of 2.74 V, J_{sc} of 8.5 mA cm^{-2}, and a FF of 86% on 1.03 cm^2.[52] For the middle- and high-bandgap perovskite solar cell, 1.55 eV $Cs_{0.1}FA_{0.9}PbI_3$ and 1.90 eV $Cs_{0.2}FA_{0.8}Pb(I_{0.45}Br_{0.55})_3$ perovskite are used, respectively. The external quantum efficiency (EQE) and integrated J_{sc} of the triple tandem devices show that the mid-gap cell limits the tandem cell current output to 8.9 mA cm^{-2}. J_{sc} can be increased to 11.9 mA cm^{-2} by optimizing the bandgap of the middle perovskite absorber to achieve better current matching. Results from current single-junction opaque solar cells show room for V_{oc} improvement for the high-bandgap cell that suffers from light-induced halide segregation. We summarized the materials and power conversion efficiencies of the perovskite/Si tandem solar cells in Table 1.

Table 1 Performance comparison of perovskite/Si tandem solar cells

Year	Materials	V_{oc} [V]	J_{sc} [mA cm^{-2}]	PCE [%]	Ref.
2016	$CH_3NH_3PbI_3$/c-Si	1.716	16.4	20.5	100
2018	$CsxFA_{1-x}Pb(I,Br)_3$/c-Si	1.786	19.5	25.2	101
2020	$Cs_{0.1}MA_{0.9}Pb(I_{0.9}Br_{0.1})_3$/c-Si	1.82	19.2	25.7	102
2022	$Cs_{0.1}FA_{0.2}MA_{0.7}Pb(I_{0.85}Br_{0.15})_3$/c-Si	1.92	18.94	28.52	105
2023	$MA(Cl_{0.5}SCN_{0.5})$/c-Si	1.85	19.8	28.6	106
2022	$(Cs_{0.05}(FA_{0.77}MA_{0.23})_{0.95}Pb(I_{0.77}Br_{0.23})_3$/c-Si	1.9	19.45	29.83	107
2023	$(FAPbI_3)_{0.83}(MAPbBr_3)_{0.17}$/c-Si	18.19	18.1	27.2	108

3.3. All-perovskite tandem solar cells

Perovskite can satisfy the bandgap range of the top cell (1.7–1.9 eV) and bottom cell (1.1–1.2 eV) of the TSCs due to its bandgap tunability.[5,83] All-perovskite TSCs are cost-effective compared to Si or CIGS-based tandem devices because both subcells can be fabricated with a solution process. To fabricate high-performance 2-T monolithic all-perovskite TSCs, it is essential to improve the efficiency and operational stability of each subcell. Similar to the WBG perovskite used in Perovskite/Si TSCs, a top subcell in all-perovskite TSCs also increases Br content to broaden the bandgap. However, a high ratio of Br brings about light-induced halide segregation, which causes large V_{oc} deficits and degradation under illumination.[104,117] Wen *et al.* report a steric engineering strategy that enables photostable 1.8 eV WBG perovskites with Br content down to 25 mol%.[118] They simultaneously incorporate larger A-site cation dimethylammonium and smaller halide chloride into the mixed-cation mixed-halide perovskites. The resulting perovskite film exhibited considerably suppressed light-induced halide segregation and trap densities due to strain relaxation. The best-performing single-junction WBG device delivered a PCE of 17.7% with a V_{oc} of 1.263 V, a J_{sc} of 17.4 mA cm^{-2}, and a FF of 79.7%. The encapsulated devices under 1 sun illumination retained 90% of their initial performance after continuous operation over 1000 h. All-perovskite TSCs that deployed the WBG perovskite achieved a high PCE of 26.2% with a V_{oc} of 2.046 V, a J_{sc} of 16 mA cm^{-2}, and a FF of 80.1%. Wang *et al.* doped Rb into the Cs-based inorganic WBG perovskite lattice to reduce the light-induced phase segregation by increasing lattice distortion. The doping of Rb with a smaller cation radius than Cs reduces the average interatomic distance between the A-site cation and I, which enhances the ion migration energy barrier and suppresses ion migration. Time-dependent photoluminescence measure-

ments under 1-sun illumination demonstrate that Rb/Cs mixed-cation perovskites show improved light stability. A single PSC device based on ~2.0 eV $Rb_{0.15}Cs_{0.85}Pb_{1.75}Br_{1.25}$ perovskite shows a PCE of 13.41% with a V_{oc} of 1.312 V. All-perovskite triple-junction solar cells employing the Rb/Cs mixed cation inorganic perovskite as a top cell achieved a PCE of 24.3% with a V_{oc} of 3.21 V.[119]

Another subcell comprising the all-perovskite TSCs, NBG perovskite with a bandgap around 1.2 eV, is obtained by alloying the tin and lead from the B-site. The main factor that adversely affects the stability and device efficiency of NBG perovskite is the oxidation of Sn^{2+} to Sn^{4+}. The formation of Sn^{2+} vacancy caused by oxidation breaks the charge neutrality of the perovskite films by self-p-doping and increases the recombination centers.[120] To suppress tin oxidation and improve the device performance, additives such as SnF_2, guanidinium thiocyanate (GuaSCN),[121] metallic tin,[122] and zwitterionic antioxidants[123] were used in the perovskite precursor solution. Lin *et al.* introduced 4-trifluoromethyl-phenyl ammonium (CF3-PA) into the NBG perovskite through molecular dynamic simulations to enhance the passivator adsorption that occurs at the defect sites on the surface.[124] CF3-PA has a highly electronegative fluorine atom that withdraws electron density from the neighboring atoms. Then the NH^{3+} side of CF3-PA becomes highly electropositive and strongly binds with the negatively charged defects, which means the effective passivation of the grain surface. The best CF3-PA mixed NBG device showed a PCE of 22.2% (stabilized 22.0%) with a V_{oc} of 0.841 V, a J_{sc} of 33 mA cm^{-2}, and a FF of 80% under reverse scan. With the 1.2-um-thick NBG subcell using CF3-PA additive, the champion tandem cell achieved 26.7% with a V_{oc} of 2.03 V, a J_{sc} of 16.5 mA cm^{-2}, and a FF of 79.9%, and certified stabilized PCE of 26.4%. The encapsulated devices in ambient air maintained 90% of their initial PCE after 600 h of MPP operation under simulated 1 sun illumination. A combination of phenethylammonium iodide (PEAI) and GuaSCN additives in Pb–Sn mixed perovskite improves the film quality and optoelectronic properties by forming quasi-2D $(PEA)_2GaPb_2I_7$, as shown in Fig. 7a.[125] An increase in carrier lifetime and remarkably reduced dark carrier density of the perovskite using the mixed additive was confirmed through the TRPL and Hall-effect measurement. The V_{oc} values of the NBG devices show an increase from 0.747 V (control) to 0.820 V (GuaSCN) to 0.883 V (GuaSCN + PEAI) from the reverse scan. The improvement of V_{oc} when using mixed additives is due to the reduced recombination associated with the low dark carrier density. The reverse scan of the champion NBG PSC yielded a PCE of 22.2%, with a V_{oc} of 0.916 V, a J_{sc} of 30.62 mA cm^{-2}, and a FF of 79%. The PCE of the best all-perovskite tandem device is 25.5% with a high V_{oc} of 2.121 V, which is attributed to the high V_{oc} of the NBG subcell (Fig. 7b and c). The unencapsulated 2-T tandem cell at 30–35 °C retained 80% of its maximum efficiency after 1500 h under continuous light illumination at ~0.8 sun. Luo *et al.* report a carrier management

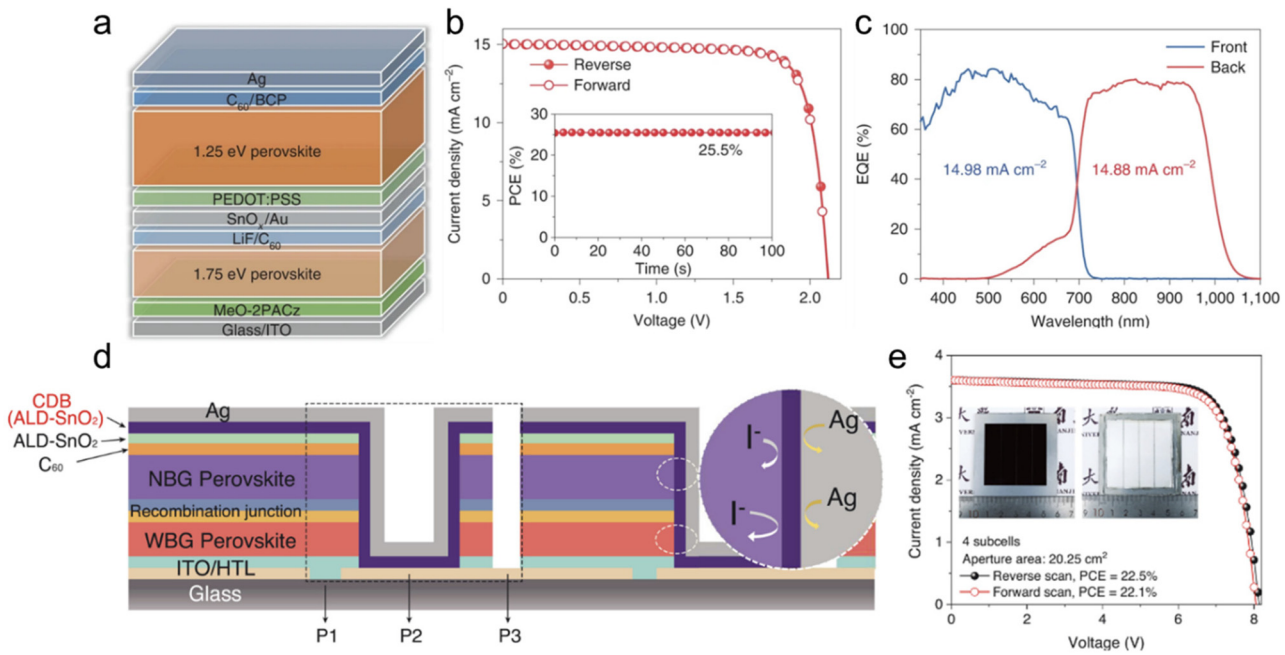

Fig. 7 All-perovskite tandem solar cells. (a) Schematic of the 2-T monolithic tandem device. (b) *J*–*V* curve of the champion all-perovskite tandem solar cell along with the stable power output efficiency near the maximum power point (inset). (c) EQE spectra of the front (wide-bandgap) and back (narrow-bandgap) subcells with the integrated J_{sc} values indicated. Reproduced from ref. 125. Copyright 2022 Nature Publishing Group. (d) Schematic diagram of the structure of the series-connected all-perovskite tandem module with CDB to prevent ion diffusion and hole transport layer (HTL). (e) *J*–*V* curves of the champion all-perovskite tandem module (aperture area of 20.25 cm^2, four subcells in series). The inset shows photos of the front side (left) and back side (right) of the module. Reproduced from ref. 135. Copyright 2022 Science.

strategy for using cysteine hydrochloride (CysHCl) to improve carrier management, which can suppress trap-assisted non-radiative recombination and promote carrier transfer.[126] CysHCl simultaneously acts as a bulky passivator and a surface anchoring agent for Sn–Pb perovskite. They introduced trace amounts of CysHCl into the NBG perovskite precursor solution and coated the CysHCl solution on top of the perovskite layer. $-NH^{3+}$ and the O/S atoms at $COOH^{-}$, which make up $CysH^{+}$, are tend to fill $FA^{+}/MA^{+}/Cs^{+}$ vacancies and passivate undercoordinated Sn^{2+}/Pb^{2+} and iodine vacancies.[127,128] The CysHCl-processed perovskite film exhibit reduced trap density and Sn^{4+} content, leading to a significantly increased carrier lifetime of 2.88 us and diffusion length of 8.67 μm. Besides, CysHCl post-treatment promotes the formation of surface dipoles and energy band bending downwards at the perovskite/C_{60} interface, which facilitates electron extraction. The PCE of 22.15% with a V_{oc} over 0.87 V and a FF over 81% is obtained in NBG PSCs with doping and post-treatment of CysHCl. Combining the CysHCl-processed NBG with a WBG (1.77 eV) perovskite top subcell, a certified PCE of 2-T all-perovskite TSC reached 25.7%. The encapsulated TSC maintained 80% of its original PCE for about 327 h of MPP tracking. Wang *et al.* developed a universal close-space annealing (CSA) strategy by placing the intermediate-phase perovskite films with their faces towards solvent-permeable covers during the annealing process.[129] The CSA process prevents the internal solvent from quick escape to slow the crystallization and enables the remaining solvents to dissolve the grain boundaries to enlarge grain size. CSA-processed NBG and WBG films showed enhanced crystallinity and prolonged carrier lifetimes, indicating that trap density is reduced. The CSA-based PSCs have a V_{oc} of 0.856 V, a J_{sc} of 31.29 mA cm^{-2}, and a FF of 80.1%, yielding a PCE of 21.51% under reverse scan. The best-performing CSA-based 2-T all-perovskite TSC obtains the PCE of 25.5% under reverse scan, with a V_{oc} of 1.956 V, a J_{sc} of 15.41 mA cm^{-2}, and a FF of 83.1%, which are much higher than the normal annealing-based tandem device with a PCE of 22.49%, a V_{oc} of 1.926 V, a J_{sc} of 14.54 mA cm^{-2}, and a FF of 80.3% under reverse scan.

As mentioned so far, the all-perovskite TSC show a high certified PCE of up to 28%, improving various problems they have.[91] However, these results were obtained for small-area devices of less than 1 cm^2 using the spin coating technique. Methods such as blade coating,[86,130] slot-die coating,[131,132] spray coating,[133] and inkjet printing[134] have been studied to fabricate large-area perovskite films and further develop high-efficiency perovskite-based tandem solar modules. In particular, large-area fabrication of 1.8 eV WBG perovskite films is required for the modularization of all-perovskite TSCs. The solvent system used for scalable coating of a state-of-the-art 1.5 eV perovskite film is not compatible with the fabrication of 1.8 eV perovskite film with high bromide content due to the low solubility of lead and cesium bromide salts. To solve these problems, Xiao *et al.* controlled the crystal nucleation rate by finely tuning the Cs content to improve the uniformity of blade-coated perovskite films over large areas with a bandgap of 1.8 eV.[135] They fabricated the 1.8 eV perovskite film with a large grain size and flat surface with a blade coating by increasing the Cs content to 35 mol%. Using this scalable process technique, they obtained a PCE of 24.8% with a V_{oc} of 2.025 V, a J_{sc} of 15.4 mA cm^{-2}, and a FF of 82.6% for a 1.05 cm^2 area all-perovskite tandem device. In addition, to increase the long-term stability of the device, they deposited a conformal diffusion barrier (CDB) layer consisting of an atomic layer deposited SnO_2 after P2 scribing in the all-perovskite tandem solar module, as shown in Fig. 7d. CDB layer acts as a lateral diffusion barrier that inhibits the reaction between perovskite and metal electrode and serves as a vertical electron extractor to connect each subcell in series in the all-perovskite tandem solar module. A champion tandem module with the CDB layer exhibited a certified PCE of 21.7% in a 20.25 cm^2 aperture area, as shown in Fig. 7e. The tandem module also retained 75% of its initial efficiency after 500 hours of continuous operation under simulated 1-sun illumination in ambient conditions. He *et al.* developed a novel self-assembled monolayer (SAM) with (4-(7*H*-dibenzo[*c*,*g*]carbazol-7-yl)butyl)phosphonic acid (4PADCB) as a hole-selective layer for high-quality WBG PSCs over a large area.[136] They introduced two benzene rings into the carbazole group of the commercial [4-(9*H*-carbazol-9-yl)butyl]phosphonic acid (4PACz) to improve the incomplete coverage and surface wettability of the SAM over TCO that causes the relatively low FF in large-area devices. Photo-induced force microscopy demonstrates that 4PADCB has a more homogenous anchoring on TCO than 4PACz due to the special steric hindrance of the 7*H*-dibenzocarbazole terminal group. The 4PADCB also suppressed the interfacial non-radiative recombination loss and enabled the fabrication of 1.05 cm^2 all-perovskite TSC of a certified PCE of 26.6% with a V_{oc} of 2.12 V and a FF of 82.6%. We summarized the materials and power conversion efficiencies of the all-perovskite tandem solar cells in Table 2.

4. Electrocatalysts for halide perovskite PV-EC fuel generation

4.1. Oxygen evolution catalysts

As mentioned earlier, the oxygen evolution reaction involving 4 electrons requires a higher overpotential than the hydrogen evolution reaction, determining the overall water splitting rate. Therefore, many studies have been conducted to reduce the OER overpotential using various strategies such as morphology, composition, and interface control.[137] Mainly, transition metals with partially filled d orbitals are used as constituent elements because of fast electron transfer and high catalytic activity for OER.[138] In particular, through the compositional optimization of various non-noble metals, a higher catalytic activity than that of rare earth metals such as Ir and Ru was implemented.[139,140]

First, high-entropy alloys (HEAs) based on transition metals are representative materials for the oxygen evolution catalyst. The HEAs with maximized configurational entropy by alloying 4 or more elements have extraordinary electrochemical pro-

Table 2 Performance comparison of all-perovskite tandem solar cells

Year	Materials	V_{oc} [V]	J_{sc} [mA cm^{-2}]	PCE [%]	Ref.
2022	$DMA_{0.1}Cs_{0.4}Br_{0.25}Cl_{0.05}/MA_{0.3}FA_{0.7}Pb_{0.5}Sn_{0.5}I_3$	2.046	16	26.2	118
2019	$Cs_{0.05}FA_{0.8}MA_{0.15}PbI_{2.55}Br_{0.45}/(FASnI_3)_{0.6}(MAPbI_3)_{0.4}$	1.942	15.01	23.4	121
2019	$Cs_{0.2}FA_{0.8}PbI_{1.8}Br_{1.2}/Cs_{0.05}MA_{0.05}FA_{0.9}PbI_{2.85}Br_{0.15}$	1.965	15.6	24.8	122
2020	$Cs_{0.2}FA_{0.8}PbI_{1.8}Br_{1.2}/FA_{0.7}MA_{0.3}Pb_{0.5}Sn_{0.5}I_3$	2.013	16.0	25.6	123
2022	$FA_{0.8}Cs_{0.2}Pb(I_{0.62}Br_{0.38})_3/FA_{0.7}MA_{0.3}Pb_{0.5}Sn_{0.5}I_3$	2.03	16.5	26.7	124
2022	$FA_{0.7}Cs_{0.3}PbI_{2.1}Br_{0.9}/(FASnI_3)_{0.6}(MAPbI_3)_{0.4}$	2.121	15.03	25.5	125
2023	$FA_{0.8}Cs_{0.2}Pb(I_{0.6}Br_{0.4})_3/FA_{0.6}MA_{0.3}Cs_{0.1}Pb_{0.5}Sn_{0.5}I_3$	2.079	15.44	26.02	126
2022	$FA_{0.8}Cs_{0.2}Pb(I_{0.7}Br_{0.3})_3/(FASnI_3)_{0.6}(MAPbI_3)_{0.4}$	1.956	15.41	25.05	129
2022	$Cs_{0.35}FA_{0.65}PbI_{1.8}Br_{1.2}/MA_{0.3}FA_{0.7}Pb_{0.5}Sn_{0.5}I_3$	2.025	15.4	24.8	135
2023	$FA_{0.8}Cs_{0.2}Pb(I_{0.6}Br_{0.4})_3/FA_{0.6}MA_{0.3}Cs_{0.1}Sn_{0.5}Pb_{0.5}I_3$	2.09	15.41	26.47	136

perties by enhanced active sites from strain effects or interparticle distances.[141–143] Yet, HEAs, which require the same ratio of elements to exceed the configurational entropy of 1.5 R, have limitations in searching for the optimal composition for OER. In this flow, Park *et al.* adopted medium-entropy alloys (MEAs) to achieve high catalytic properties and stabilities.[144] As shown in Fig. 8a, the optimized $Fe_{60}(CoNi)_{30}Cr_{10}$ MEA was found, and its catalytic activity was further improved through anodizing and cyclic voltammetric (CV) activation. Anodizing is an electrochemical method for fabricating nanostructures with maximized surface area by oxidizing metal thin films. The CV-activated MEA with the overpotential of 187 mV was combined with a Pt cathode and a perovskite/Si tandem solar cell and recorded a remarkable STH conversion efficiency of 20.7% (Fig. 8b).

Layered double hydroxides (LDHs) are one of the most promising oxygen evolution catalyst materials because of their high conductivity, multiple oxidation states, high redox activity, and large surface areas.[145,146] For the PV-EC cell, Li *et al.* adopted NiFe LDHs on carbon nanotubes (CNTs) as an anode with an overpotential of 220 mV.[147] It is noteworthy that the anode was combined with an efficient monolithic perovskite/organic tandem solar cell (PCE of 15.13%, V_{oc} of 1.85 V, and J_{sc} of 11.52 mA cm^{-2}). The PV-EC device demonstrated a STH conversion efficiency of 12.30% and 11.21% with rigid and flexible perovskite/organic tandem solar cells, respectively.

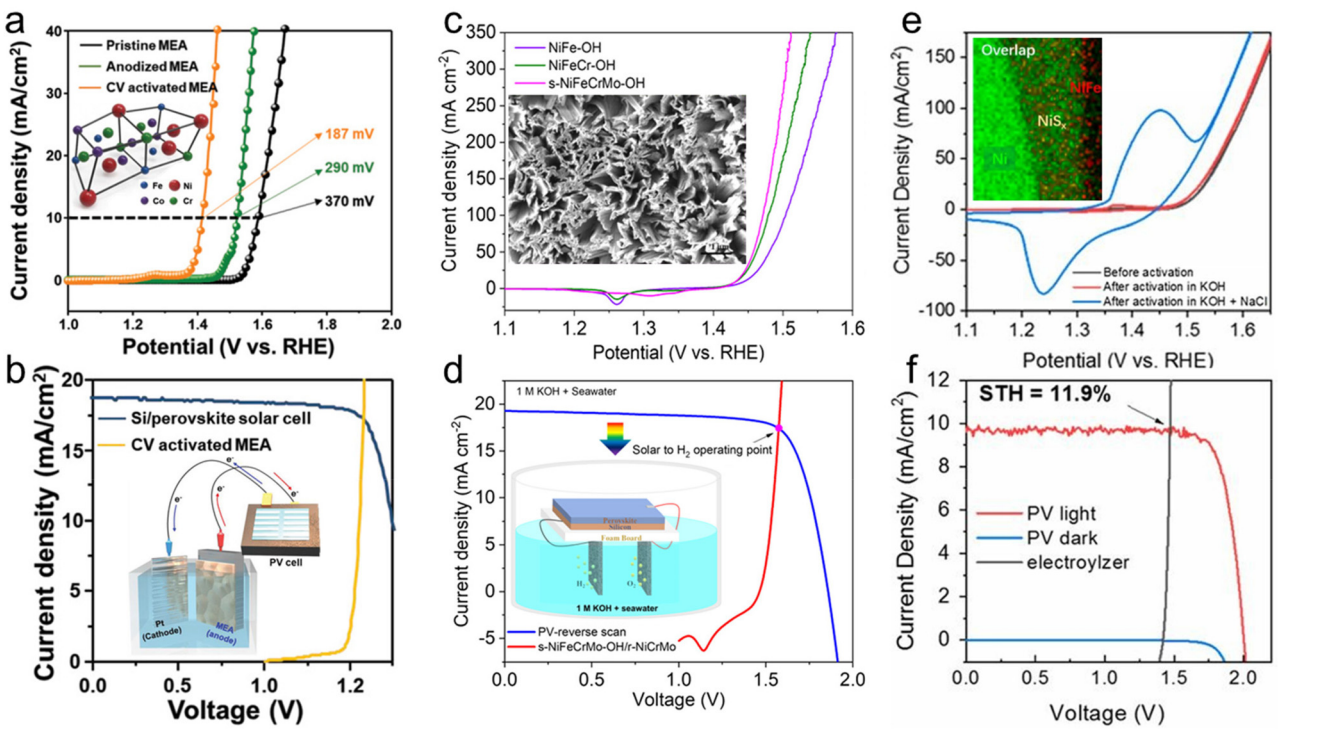

Fig. 8 Oydrogen evolution catalysts for PV-EC devices. (a) *J*–*V* curves of $Fe_{60}(CoNi)_{30}Cr_{10}$ medium-entropy alloys (MEAs) and (b) *J*–*V* curves for the perovskite/Si tandem solar cell–MEA anode//Pt cathode. Reproduced from ref. 144. Copyright 2022 Wiley. (c) *J*–*V* curves of s-NiFeCrMo-OH and (d) *J*–*V* curves for the perovskite/Si tandem solar cell–s-NiFeCrMo-OH anode//r-NiCrMo cathode. Reproduced from ref. 153. Copyright 2023 American Chemical Society. (e) *J*–*V* curves of NiFe/NiS_x on NF and (f) *J*–*V* curves for the two tandem perovskite solar cell–NiFe/NiS_x/NF anode//Ni-NiO-Cr_2O_3 cathode. Reproduced from ref. 164. Copyright 2019 *PNAS*.

The introduction of trimetallic or multimetallic hydroxides can further expedite the oxygen evolution reaction kinetics. Also, metal–organic frameworks (MOFs) have been widely used as precursors for multi-component catalysts due to their high surface area, tailorable structure, and compositional diversity.[148,149] Pan *et al.* introduced the MOF nanosheets through the hydrothermal reaction of metal thiophenedicarboxylic acid (TDC).[150] Hydrothermal synthesis can promote the formation of catalysts with high surface area and crystallinity, which provides more active sites and promotes efficient charge transfer.[151,152] NiCoFe-TDC-MOF was transformed into amorphous NiCoFe hydroxide through the electrochemical CV activation. This self-reconstruction process of changing active sites of metal maximized catalytic performances. The optimized NiCoFe hydroxide anode exhibited a remarkable OER overpotential of 191 mV at 10 mA cm^{-2}. The anode was paired with $NiMo_4/MnO_{3-x}$ cathode and a monolithic perovskite/Si tandem solar cell. This PV-EC device recorded a STH conversion efficiency of 21.32%, which is the highest level in existence. Recently, Pan *et al.* also designed a quaternary metal hydroxide catalyst.[153] The hydrothermally synthesized quaternary NiFeCrMo-OH on NF is activated into s-NiFeCrMo-OH through *in situ* electrochemical treatment. As shown in Fig. 8c, the Mo element leaching during CV activation resulted in enhanced OER activity by the formation of a higher valence state as well as morphology transition to nanosheet form. The 2D nanosheet catalyst required only a low overpotential of 300 mV to reach an industrial current density of 500 mA cm^{-2}. Also, overall water splitting was realized by combining the s-NiFeCrMo-OH/NF anode with a ternary NiCrMo alloy cathode. It is remarkable that the electrolyzer generated the industrial current density of 500 mA cm^{-2} for over 1000 h at a low voltage of 1.82 V in practical seawater splitting. As shown in Fig. 8d, a floating seawater splitting device was fabricated by connecting the electrolyzer and the perovskite/Si tandem solar cell. The floating device showed a STH conversion efficiency of 20.61%, which is the highest value in solar seawater splitting.

As presented in the OER volcano plot (Fig. 4a), Ni- and Co-based oxides are promising candidates with catalytic performance comparable to IrO_2 or RuO_2. There have been many attempts to develop highly efficient noble metal-free oxide catalysts.[154,155] In particular, layered oxides containing alkaline metal such as Li, Na, and K is characterized in that they can achieve fast OER kinetics by adjusting valence states through the extraction of alkaline metal.[156,157] Weng *et al.* designed a new layered $Na_{1-x}Ni_yFe_{1-y}O_2$ double oxide electrocatalyst. The composition-controlled layered oxides were synthesized by the calcination method of oxide powders with a stoichiometric ratio.[158] The optimal $Na_{0.08}Ni_{0.9}Fe_{0.1}O_2$ catalyst exhibited a stable overpotential of 270 mV for 40 h. The performance originated the partial extraction of Na cations, which caused exposure of more MO_6 octahedra active sites to the electrolyte. The anode was also combined with NiP cathode having an overpotential of 150 mV at 10 mA cm^{-2}, and the PV-EC device was fabricated by using a 2 series-connected perovskite solar cell. This system delivered an operating current density of 9.12 mA cm^{-2}, corresponding to a STH conversion efficiency of 11.21%.

Because of their rich composition, distinctive lattice structures, and effective electron transport, transition metal sulfides have good OER characteristics.[159–161] Through the fast redox reaction, sulfur atoms can create S–S bonds, making a flexible phase structure that is favorable for electron transfer.[162] Wang *et al.* synthesized a heterostructured Co_9S_8@MoS_2 OER catalyst by sulfurization of PMo_{12}-embedded ZIF-67 precursors.[163] The synergistic interface between Co_9S_8 and MoS_2 contributed to achieving a low overpotential of 242 mV at 10 mA cm^{-2}, which surpassed that of the commercial RuO_2 catalyst (320 mV). By employing the commercial Pt/C cathode, the heterostructured Co_9S_8@MoS_2 anode was used to construct overall water splitting device. After the fabrication of the PV-EC system with the monolithic series connected perovskite solar cell, a high STH conversion efficiency of 13.6% was yielded without external bias. Heterogeneous catalysts, which induced synergistic effects by combining the aforementioned materials, also had a high OER activity. Kuang *et al.* formed NiS_x through the surface sulfurization of NF and then synthesized NiFe/NiS_x/NF (N^3) heterogeneous catalyst by electrodeposition of NiFe.[164] Electrodeposition is a feasible method for fabricating nanostructures using diverse materials due to its simplicity and ease of reaction control. It also enables the dimension control and 3D conformal coating of the catalysts to increase the catalytic activity.[145] As shown in Fig. 8e, it was confirmed that NiS_x and NiFe were uniformly formed on the NF surface. After CV activation, only about 300 mV was required to reach the industrial current density of 400 mA cm^{-2}. It is noteworthy that the N^3 anode showed higher OER characteristics in the simulated seawater. Also, since it could be operated for 1000 h without any degradation in real seawater, the heterogeneous N^3 anode was adopted for seawater splitting electrolyzer with a Ni–NiO–Cr_2O_3 cathode (overpotential of 370 mV at 500 mA cm^{-2}). The seawater electrolyzer recorded the industrial current density under 2.1 V in real seawater. As shown in Fig. 8f, the electrolyzer was connected with two perovskite tandem solar cells, and the PV-EC devices generated a STH conversion efficiency of 11.9% for seawater splitting.

Finally, some studies have simultaneously reduced the loading amount of noble elements and improved the catalytic properties. For example, Shi *et al.* designed an oligomeric molecular anode consisting of RuPol molecular complex and CNT.[165] It is important that an extremely small amount of 16 nmol cm^{-2} of Ru was loaded onto the CNT. The CV activation made the slope of the *J–V* curve for the RuPol/CNT/FTO anode sharper by maximizing the active sites, and a low overpotential of 350 mV was exhibited. The PV-EC comprising RuPol/CNT/FTO anode, Pt cathode, and perovskite solar cell generated a STH conversion efficiency of 13.2%.

4.2. Hydrogen evolution catalysts

As shown in the volcano plot for hydrogen evolution reaction (Fig. 4b), metallic elements with high catalytic activity, such as Pt, Rh, Ir, and Re, have low earth abundance. In this respect,

single-atom catalysts[166,167] and metal alloying[168,169] for HER have been actively studied to reduce the amount of noble metals. In water splitting using PV-EC devices, many studies also have concentrated on engineering bi- or multimetallic alloys to lower the noble metal contents and overpotentials.

Among the transition metals, the most promising hydrogen evolution catalyst is the NiMo alloy. Park *et al.* synthesized the Ni_4Mo films onto the NiFe alloy films by using direct electrodeposition, as shown in Fig. 9a.[170] The optimized Ni_4Mo film cathode recorded a small overpotential of 100 mV at 10 mA cm^{-2} and a low Tafel slope of 22.2 mV dec^{-1} in 1 M NaOH, which is lower than those of a Pt plate (overpotential of 130 mV). The Ni_4Mo cathode was combined with an anodized NiFe anode and a perovskite/Si tandem solar cell to form a PV-EC device. As shown in Fig. 9b, the PV-EC cell recorded an operating current density of 14.24 mA cm^{-2}, corresponding to a STH conversion efficiency of 17.52%. Similarly, Wang *et al.* fabricated Ni_4Mo hydrogen evolution catalyst on NF using the hydrothermal method.[171] The Ni_4Mo/NF catalysts presented extremely low overpotentials of 6 and 70 mV at 10 and 100 mV cm^{-2}. This performance improvement was caused by the maximized specific surface area of NF. Also, the Ni_4Mo/NF cathode constituted the overall water splitting cell with the electrodeposited NiFe/NF anode. The integrated system of the NiFe/NF anode and Ni_4Mo/NF cathode with the perovskite/Si tandem solar cell generated an operating current density of 16.27 mA cm^{-2} and a remarkable STH conversion efficiency of 20.01%.

In general, in HER, sulfides and phosphides show higher catalytic activity than hydroxides active in OER. Many studies have reported transition metal sulfides and phosphides as cathode materials.[172] Asiri *et al.* hydrothermally synthesized MoS_2 and NiS on CP.[173] MoS_2/CP cathode had a higher HER activity than NiS/CP cathode and showed an overpotential of 367 mV at 10 mA cm^{-2} in 1 M KOH. The cathode was connected with an anode of NiFe nanoparticle on CP and recorded a cell voltage of 1.9 V for 10 mA cm^{-2}. The PV-EC device with a 2-series-connected perovskite solar cell delivered a STH conversion efficiency of 12.67%. Also, Luo *et al.* fabricated CoP on Ti foil by transforming the electrodeposited $Co(OH)_2$.[174] The CoP/Ti cathode showed a low overpotential of 130 mV, and the PV-EC cell with NiFe LDH anode and 2-series perovskite solar cell retained a STH conversion efficiency of 12.7%. Bimetallic phosphides showed better HER properties. Rho *et al.* fabricated ZnO nanowires on NF and transformed them into NiMO (M = Mo, Fe, V, Co) nanowires through the cation exchange.[175] Even after phosphorization, the nanowire morphology of NiMP was maintained. In particular, it was confirmed that NiMoP had a high density of nanowires, as shown in Fig. 9c. The NiMoP/NF cathode showed a high performance with a low overpotential of 68 mV at 10 mA cm^{-2} and a Tafel slope of 87 mV dec^{-1}. Overall water splitting with a PV-EC cell was tested by combining NiFeP/NF anode and NiMoP/NF cathode with a 2 tandem perovskite solar cell. As shown in Fig. 9d. The PV-EC device generates a high STH conversion efficiency of 14%.

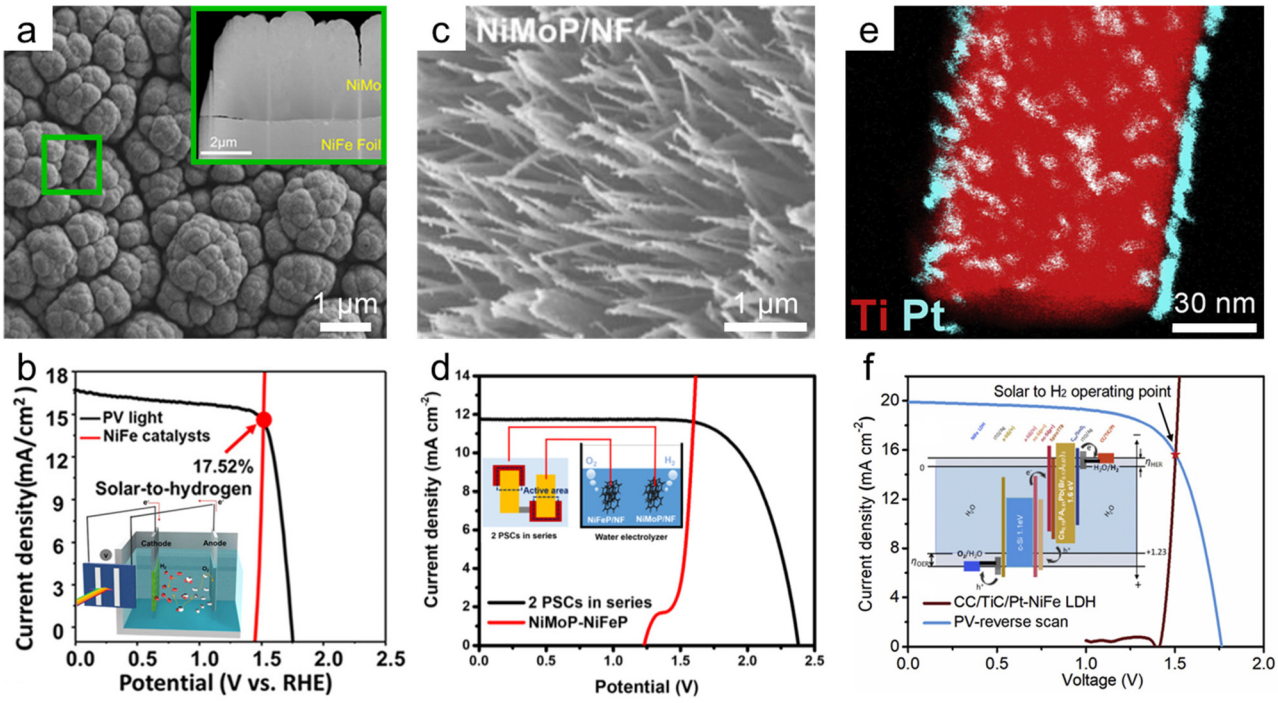

Fig. 9 Hydrogen evolution catalysts for PV-EC devices. (a) SEM images of Ni_4Mo films on NiFe foil and (b) *J*–*V* curves for the perovskite/Si tandem solar cell–NiFe-OH anode//Ni_4Mo cathode. Reproduced from ref. 170. Copyright 2019 American Chemical Society. (c) SEM image of NiMoP on NF and (d) *J*–*V* curves for the two tandem perovskite solar cells-NiFeP/NF anode//NiMoP/NF cathode. Reproduced from ref. 175. Copyright 2021 Elsevier. (e) STEM EDS chemical map of Pt/TiC on carbon cloth (CC) and (f) *J*–*V* curves for the perovskite/Si tandem solar cell–NiFe LDH anode//Pt/TiC/CC cathode. Reproduced from ref. 176. Copyright 2019 Cell Press.

HER catalyst research has also been conducted in the direction of reducing the loading amount of Pt, a noble metal. Gao *et al.* uniformly coated a small amount of Pt on the TiC nanowires using an atomic layer deposition.[176] ALD enables the formation of catalysts at the atomic layer level, allowing for intimate contact with the matrix and enhancing charge transport. Also, It can be used to design catalysts with high mass-normalized efficiency by dramatically reducing the scale and amount of the catalyst.[177] As shown in the STEM EDS map (Fig. 9e), Pt nanoclusters were anchored at the surface of TiC nanowires on CC. The Pt/TiC/CC cathode recorded remarkable overpotentials of 35 and 37 mV at 10 mA cm^{-2} in acidic and basic media, respectively. Also, the mass-normalized current density of Pt/TiC/CC (328 mA mg^{-1}) was 5 times higher than that of the Pt/C (67 mA mg^{-1}). The Pt/TiC/CC cathode was combined with NiFe LDH anode and perovskite/Si tandem solar cell, as shown in Fig. 9f. The PV-EC device delivered a high STH conversion efficiency of 18.7%.

4.3. Bifunctional electrocatalysts for water splitting

In water splitting, bifunctional electrocatalysts in which one material is used for both OER and HER have raised much research interest. Bifunctional electrocatalysts can reduce the cost of catalyst manufacturing and simplify the reaction systems.[178,179] In general, OER and HER catalysts have high activity in based and acids, respectively, but bifunctional electrocatalysts have the advantage of ignoring this pH mismatch, raising cell design efficiency. As with the aforementioned OER and HER catalyst candidates, transition metals are the main material in the bifunctional electrocatalyst for water splitting, and their various derivatives, such as oxide,[180,181] hydroxide,[182,183] sulfide,[184,185] and phosphide,[186–188] have been actively studied.

Luo *et al.* first implemented a PV-EC device using the bifunctional electrocatalyst and halide perovskite solar cell.[26] Hydrothermally obtained NiFe LDH on NF exhibited high catalytic activities for both OER and HER in alkaline electrolyte. This electrode, composed of only earth-abundant elements, recorded overpotentials of 240 mV and 210 mV at 10 mA cm^{-2} for OER and HER, respectively, which were much lower than those of the Pt/NF electrode. In overall water splitting, it required only 1.7 V to reach a current density of 10 mA cm^{-2} and durably operated for 10 h. Two series-connected perovskite solar cell was connected to the bifunctional catalyst electrodes for unbiased overall water splitting. The PV-EC device generated an operating current density of 10 mA cm^{-2}, which corresponds to a STH conversion efficiency of 12.3%. Subsequently, bifunctional electrocatalysts based on transition metal oxides were presented. Sharifi *et al.* developed large surface-area $NiCo_2O_4$ nanorods anchored in CP.[189] During the chemical vapor deposition under the NH_3 atmosphere, nitrogen-doped carbon nanotubes (N-CNT) were formed on the CP, and $NiCo_2O_4$ nanorods were synthesized on N-CNT/CP. This catalyst exhibited bifunctional properties and achieved overpotentials of 420 mV and 410 mV at 10 mA cm^{-2} for OER and HER, respectively. The $NiCo_2O_4$/N-CNT/CP electrodes were combined with the multiple connected perovskite solar cell to construct the PV-EC water splitting cell. Since V_{oc} increases and J_{sc} decreases as the number of connected PV cells, the 3-serial PV cell was the optimal structure when combined with electrodes. In this study, although the wired artificial leaf device showed not high STH conversion efficiency of 6.2%, a cost analysis was well established.

With a simple phosphorization of transition metal alloy, Baek *et al.* implemented bifunctional catalysts, which can overcome pH problems, the restriction in overall water splitting.[190] As shown in the fabrication process (Fig. 10a), Ternary NiMoFe alloys electrodeposited on Ti foil were used as HER catalyst and phosphorized to be used as OER catalyst. As noted in the HER catalyst chapter, the incorporation of Ni and Mo optimized hydrogen adsorption energy for HER and led to the NiMoFe cathode exhibiting a low overpotential of 68 mV at 10 mA cm^{-2}. Also, the incorporation of Ni and Fe expedited OER kinetics and made the NiMoFeP anode have a low overpotential of 286 mV at 10 mA cm^{-2}. An overall water splitting

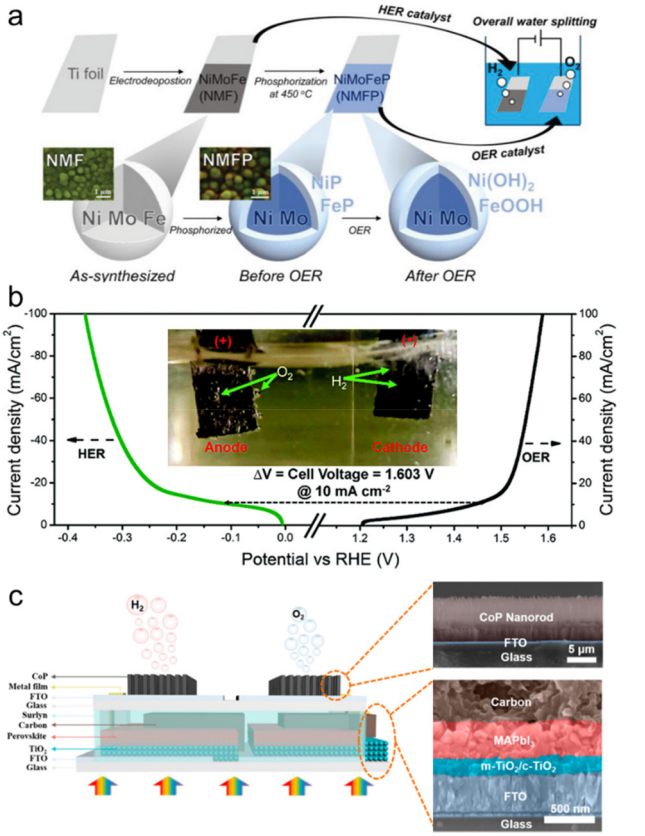

Fig. 10 Bifunctional electrocatalysts for PV-EC water splitting devices. (a) Fabrication process of overall water splitting system with NiMoFeP (NMFP) anode and NiMoFe (NMF) cathode. Reproduced from ref. 190. Copyright 2019 Wiley. (b) *J*–*V* curves of NiFe nanoparticles on N,S-doped carbon (NF-8) for the OER and HER. Reproduced from ref. 191. Copyright 2018 Royal Society of Chemistry. (c) Schematic structure of the integrated device with the two series-connected perovskite solar cells–two CoP electrodes. Reproduced from ref. 195. Copyright 2020 American Chemical Society.

system comprising NiMoFeP anode and NiMoFe cathode used a low voltage of 1.58 V to generate 10 mA cm^{-2}. In unbiased overall water splitting, the PV-EC cell connected with a tandem perovskite solar cell produced a STH conversion efficiency of 12.3%. In addition, various transition metal alloys were applied to the bifunctional electrocatalyst. Kumar *et al.* synthesized bimetallic NiFe nanoparticles by simple pyrolysis.[191] It is characteristic that the support for NiFe alloy (N, S-doped carbon matrix) was derived from the carbonization of duckweed. As shown in Fig. 10b, the NiFe/CP catalysts were utilized as both the anode for OER and the cathode for HER. Low overpotentials of 267 mV and 106 mV for OER and HER, respectively, realized a low cell voltage of 1.603 V for 10 mA cm^{-2} when forming an overall water splitting electrolyzer. After being connected with the perovskite solar cell, the electrolyzer delivered a STH conversion efficiency of 9.7%. Ekspong *et al.* introduced a trimetallic NiFeMo electrocatalyst anchored to a nitrogen-doped CNT.[192] When Fe and Mo are combined with Ni, the OER and HER are improved, respectively, so the trimetallic system showed better bifunctional electrocatalysis than the previous bimetallic system. In particular, the NiFeMo/CNT showed improved characteristics due to the increase in specific surface area by the nanostructures and recorded a low total overvoltage of 450 mV at 10 mA cm^{-2}. Due to the trimetallic alloying, the PV-EC system recorded a high STH conversion efficiency of 13.8% after combining it with a 2-series perovskite solar cell.

Transition metal phosphide is one of the most widely used bifunctional catalyst materials. Ma *et al.* first applied a metal phosphide-based bifunctional catalyst to the PV-EC system.[193] Hydrothermally synthesized NiCo-precursor on CP was transformed into NiCoP/CP electrode. Since the phosphide nanowires offered abundant active sites, the NiCoP/CP electrode recorded overpotentials of 260 mV and 43 mV at 10 mA cm^{-2} for OER and HER, respectively, which is comparable to existing noble metal catalysts. An electrolyzer consisting of NiCoP/CP electrodes needed only 1.61 V to generate 10 mA cm^{-2}. The PV-EC system delivered a STH conversion efficiency of 3.12% when combined with an all-inorganic perovskite solar cell. Xiao *et al.* implemented the bifunctional catalysis of Ni_5P_4 by introducing a hydrazine oxidation as an alternative reaction to OER for hydrogen production.[194] The hydrazine oxidation with −0.33 V_{NHE} has attracted attention as an easy oxidation reaction in anode compared to OER. Ni_5P_4 showed a high hydrazine oxidation activity after the phosphorization from $Ni(OH)_2$ and recorded a low overpotential of 51 mV at 10 mA cm^{-2}, which is much smaller than that of the commercial Pt/C (172 mV). Also, in HER, phosphide was more active than hydroxide, showing an overpotential of 94 mV at 10 mA cm^{-2}. Moreover, at the matched operating point of the electrolyzer with the maximum power point of the PV cell, a perovskite solar cell could operate three reformed electrolyzers in series for hydrogen evolution with a rate of 1.77 mg h^{-1} production. Liang *et al.* implemented a type II PV-EC cell using CoP bifunctional electrocatalysts that can be synthesized with a simple solution process (Fig. 10c).[195] As mentioned in the previous chapter, the catalyst monolithically combined with the solar cell has the advantage of simplifying the whole system. The CoP nanorods derived by hydrothermal method require OER and HER overpotentials of 390 mV and 188 mV, respectively, to reach 10 mA cm^{-2}, which is lower than that of cobalt oxide. Overall water splitting was operated with the type II PV-EC cell composed of bifunctional CoP catalyst electrodes and perovskite tandem solar cell, displaying a STH conversion efficiency of 6.7%.

Finally, carbon-based materials were also applied to bifunctional water splitting catalysts. Hu *et al.* synthesized N, S co-doped 3D porous graphitic network (N, S-3DPG) through the carbonization of the precursor with melamine and thiourea.[196] The N, S-3DPG was more advantageous to OER, showing a low overpotential of 310 mV at 10 mA cm^{-2}, which is comparable to that of RuO_2 (300 mV). It resulted from enhanced electron transfer due to N and S elements that create multiple active sites on the carbon skeleton. The N, S-3DPG catalyst electrodes were combined with a 3-series perovskite solar cell, generating a high STH conversion efficiency of 11.7%.

We summarized the structures and STH conversion efficiencies of the perovskite PV-EC water splitting devices in Table 3. In order to achieve sufficient photovoltage, most photovoltaic cells are composed of perovskite-based tandem structures. Additionally, it can be observed that transition metals dominate for electrocatalysts. To achieve a higher STH conversion efficiency of over 20%, the development of perovskite solar cells with high PCE and electrocatalysts with low overpotential is essential.

4.4. CO_2 reduction catalysts

The synthesis of hydrocarbons *via* the electroreduction of CO_2 from solar energy is an attractive strategy for storing high-

Table 3 Performance comparison in the STH conversion efficiency of PV-EC devices for water splitting

Year	Solar cell	Anode	Cathode	η_{STH} [%]	Ref.
2020	2PSC	Ru(O)Pol/CNTs/FTO	Pt	13.2	165
2023	PSC/Si	s-NiFeCrMo-OH/NF	r-NiCrMo/NF	20.6	153
2020	PSC/OPV	NiFe/CNT	Pt/C	12.3	147
2022	2PSC	Co_9S_8@MoS_2/CC	Pt/C	13.6	163
2017	2PSC	$Na_{0.08}Ni_{0.9}Fe_{0.1}O_2$/NF	NiP/NF	11.2	158
2021	PSC/Si	NiCoFe-TDC-AC/NF	$NiMo_4/MnO_{3-x}$/NF	21.3	150
2019	2PSC	NiFe/NiS_x/NF	Ni-NiO-Cr_2O_3/NF	11.9	164
2022	PSC/Si	$Fe_{60}(CoNi)_{30}Cr_{10}$	Pt	20.6	144
2019	PSC/Si	NiFe-OH/NiFe	Ni_4Mo/NiFe	17.5	170
2016	2PSC	NiFe LDH/NF	CoP/Ti	12.7	174
2021	PSC/Si	NiFe/NF	NiMo/NF	20.0	171
2021	2PSC	NiFeP/NF	NiMoP/NF	14.3	175
2022	2PSC	NiFe/CP	MoS_2/CP	12.7	173
2019	PSC/Si	NiFe LDH/NF	Pt/TiC/CC	18.7	176
2020	2PSC	CoP/FTO	CoP/FTO	6.7	195
2021	2PSC	NiFeMo/CP	NiFeMo/CP	13.8	192
2016	3PSC	$NiCo_2O_4$/N-CNT/CP	$NiCo_2O_4$/N-CNT/CP	6.2	189
2019	PSC	Ni_5P_4/CC	Ni_5P_4/CC	5.4	194
2018	PSC	NiFe/CP	NiFe/CP	9.7	191
2018	PSC	NiCoP/CP	NiCoP/CP	3.1	193
2017	3PSC	N,S-3DPG/CF	N,S-3DPG/CF	11.7	196
2014	2PSC	NiFe LDH/NF	NiFe LDH/NF	12.3	26
2019	2PSC	NiMoFeP	NiMoFe	12.3	190

density energy. However, light-driven CO_2 reduction is still challenging to reach high STF conversion efficiency because the operating voltage over 2.5 V is required due to the overpotential. To produce enough V_{op} and J_{op}, the perovskite solar cells are used as 3 or more series-connected and/or parallel-connected modules. Schreier *et al.* first reported a solar-to-CO conversion efficiency of 6.5%, connecting only series-connected perovskite photovoltaic with high-efficiency Au and IrO_2 electrodes under a real load condition (Fig. 11a).[197] Oxidized Au cathodes with a highly porous structure were prepared by electrochemical anodization to enhance the catalytic performance. The 3 series-connected perovskite solar cell showed V_{oc} of 3.1 V and J_{sc} of 6.15 mA cm^{-2}. And the V_{op} is 5.93 mA cm^{-2} was well matched with intersecting of the perovskite *J–V* characteristic and electrochemical cell (Fig. 11b). Moreover, the light-driven CO_2 reduction cell shows high stability for 18 h with the faradaic efficiency varying of 80% and 90%. Esiner *et al.* reported a solar-to-CO conversion efficiency of 8.3% by the Au and RuO_2 electrodes connected with 3 series-connected photovoltaic cells (Fig. 11c).[198] The Au wire as the electrode for CO production had a diameter of 1 mm and high purity of 99.9999%, and the hydrothermally synthesized RuO_2 electrodes were deposited on Ti substrates for CH_4 production. The 3-cell module has an PCE of 17.4% and FF of 0.81 (V_{oc} of 3.05 V, J_{sc} of 7.0 mA cm^{-2}) under AM 1.5G illumination. The electrochemical cell required cell voltages of 2.5 V and 3 V for efficient CO_2 reduction to CO and CH_4, respectively. (Fig. 11d). Appropriate balancing that controlled the operating current (I_{OP}) to 2 mA was necessary since the increased current introduced high resistive losses in the cell. As a result, the solar-to-CH_4 conversion efficiency is estimated to be 2% with a faradaic efficiency of 40%.

Zhang *et al.* reported high solar-to-CO conversion efficiency of 12.5% by single-atom metals anchored Zr-cluster-porphyrin framework hollow nanocapsules (M-SAs/Zr-CPF) connected with a custom-built large area perovskite solar cell (Fig. 12a).[199] Among various metals, the Co single atoms of Co-SAs/Zr-CPF showed enhanced catalytic activity by the favorable formation step of the *COOH and desorption step of the *CO intermediate. The large area perovskite solar cell has an PCE of 21.3% with V_{oc} of 4.6 V and J_{sc} of 8.96 mA cm^{-2} under AM 1.5G illumination. The V_{OP} of 3.2 V and I_{OP} of 3.2 mA was determined by the intersection point of the current–voltage (*I–V*) curve of the perovskite solar cell and the polarization curve of the electrochemical cell (Fig. 12b). Moreover, the light-driven electrocatalysis system showed no obvious degradation in long-term stability tests for 10 h. Huan *et al.* reported a low-cost system with a solar-to-C^2 hydrocarbon (ethane and ethylene) efficiency of 2.3% by dendritic nanostructured copper oxide material catalyst (DN-CuO) as both the anode and cathode connected with two series of three perovskite solar cells module (Fig. 12c).[200] In addition, to overcome mass transfer of CO_2 to the cathode surface, a continuous-flow electrochemical cell in which the 0.1 M $CsHCO_3$ anolyte and catholyte with constant saturation in CO_2 was used at the system. The perovskite solar cell minimodule shows an PCE of 17.6% at 2.45 V under AM 1.5G illumination (Fig. 12d). For the optimal match between the *I–V* characteristic of the electrolyzer cell and the minimodule, the geometric surface areas of

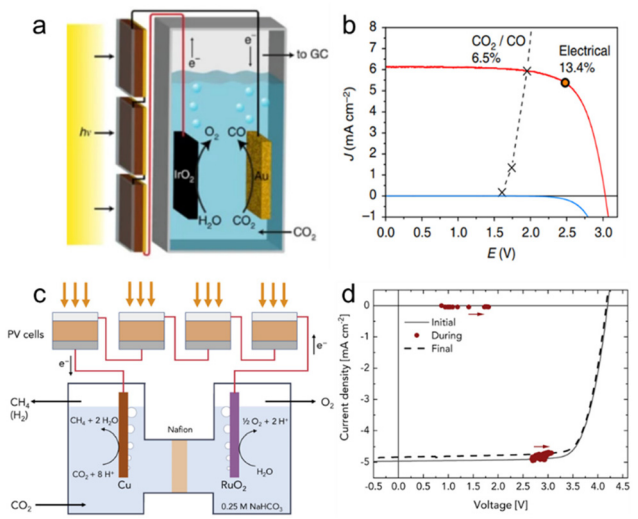

Fig. 11 CO_2 reduction catalysts for PV-EC devices. (a) Schematic of the device combining photovoltaics with and electrochemical cell. (d) *J–V* curves of three series-connected perovskite solar cells overlaid with the matched *J–V* characteristic of the CO_2-reduction and oxygen-evolution electrodes. Reproduced from ref. 197. Copyright 2015 Nature publishing group. (c) Schematic of the light-driven electrochemical device for reduction of CO_2 to CH_4. (d) *J–V* curves of 4 series-connected perovskite solar cells before, during, and after 510 nm light-driven CO_2 reduction. Reproduced from ref. 198. Copyright 2019 Cell Press.

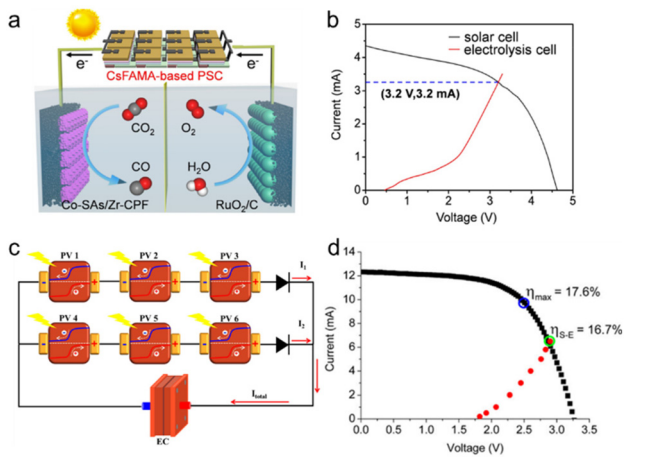

Fig. 12 Halide perovskite PV-EC devices for solar hydrocarbon generation. (a) Schematic illustration of the integrated solar-driven CRR-OER electrolysis system powered by a homemade large-area CsFAMA-based perovskite solar cell. (b) *J–V* curves for large-area CsFAMA-based perovskite solar cell–RuO_2/C anode//Co-SAs/Zr-CPF cathode. Reproduced from ref. 199. Copyright 2022 American Chemical Society. (c) Schematic diagram of the perovskite module connected to the electrolyzer. (d) *J–V* characteristic of the perovskite minimodule and measured operating current of the electrolyzer. Reproduced from ref. 200. Copyright 2019 *PNAS*.

Table 4 Performance comparison in the STF conversion efficiency of PV-EC devices for CO_2 conversion

Year	Solar cell	Anode	Cathode	η_{STF} [%]	Ref.
2020	3PSC	RuO_2/Ti	Au	CO: 8	198
2022	4PSC	RuO_2/C	Co-SAs/Zr-CPF	CO: 12.5	199
2015	4PSC	IrO_2/Ti	Au	CO: 6.5	197
2019	2PSC	CuO	CuO	C_2H_4, C_2H_6: 2.3	200

the cathode and the anode were adjusted to 0.35 and 0.85 cm^2, respectively. As a result, ethane and ethylene were obtained as the main products with an average faradaic efficiency of 40.5%, together with CO and HCOOH of 4.8% and 6.4%, respectively. We summarized the structures and STF conversion efficiencies of the perovskite PV-EC CO_2 conversion devices in Table 4. Light-driven CO_2 reduction research suffers from high overpotential of the electrode, selective synthesis of products, side reaction of dissolved products, and coupling electrolyzer to solar cell module with high electrical loss. Despite several problems, there is still room for improvement. The use of more advanced electrodes and the rapid development of perovskite solar cells will solve the problems for industrial applicability with low cost and high efficiency.

5. Summary and outlooks

The demand for sustainable energy sources is growing rapidly due to increasing concerns about climate change and the need to reduce our reliance on fossil fuels. As the one promising solution, solar fuel generation which produces hydrogen and hydrocarbon using solar energy, has been studied in various ways. In this review, we mainly dealt with the recent progress of halide perovskite photovoltaic-electrochemical (PV-EC) fuel production, which combines solar energy conversion and electrocatalysis. Halide perovskite solar cells with adjustable band gaps were presented with various tandem solar cell types. We also explained the basic of electrocatalysis for the OER, HER, and CRR. We highlighted the structural, compositional, and interfacial engineering of OER, HER, bifunctional, CRR catalysts, and halide perovskite solar cells in recent PV-EC water splitting and CO_2 conversion to improve the STF conversion efficiency. This review contributed to suggesting a comprehensive overview of the state-of-the-art halide perovskite PV-EC fuel generation. Also, this work offered discussions about significant advances in PV-EC fuel production from a materials point of view, providing a groundwork for its component design.

Halide perovskite-based solar cells have made remarkable progress in a few years and paved a promising path to solving many problems. As a result, the certified highest efficiencies of 31.3% and 28% were achieved in perovskite/Si and all-perovskite tandem solar cells, respectively.[91] For the stable operation of the PV-EC system, it is necessary to secure long-term stability while improving the efficiency of the perovskite-based solar cells. A typical problem that prevents the stable device operation is a large V_{oc} deficit caused by the light-induced phase segregation in WBG perovskite. This phase separation reduces the V_{oc} of the WBG single junction devices and the tandem devices, making them unable to produce sufficient voltage for the PV-EC systems and adversely affecting the operational stability. Methods such as reducing the Br content through cation engineering and defect passivation of various additives have been studied to solve the problem.[105,118] Breakthroughs such as the development of pure-iodide-based WBG perovskites are essential for the dramatic enhancement of the device's stability.

In electrocatalysis, significant performance improvements have also been made based on structural, compositional, and interfacial engineering. For practical use of PV-EC fuel production, advances in electrocatalysts are still required from the material point of view, which is a revolutionary reduction of the stagnant overpotential. The search for new electrocatalytic materials is essential with a focus on finding more efficient and cost-effective options. This includes the development of new transition metal-based catalysts, as well as the investigation of hybrid materials that combine the best properties of multiple materials. Also, single-atom catalysts that increase mass-normalized efficiency by controlling the content of noble metals at the atomic level are promising. Furthermore, future research should focus on developing materials that can withstand harsh operating conditions for longer periods, such as in acidic or alkaline environments. The use of advanced characterization methods and computational modeling can help researchers gain a deeper understanding of the mechanisms behind electrocatalysis and guide the design of new materials with improved properties.

Author contributions

Jin Wook Yang: conceptualization, investigation, visualization, writing (original draft, review & editing). You Jin Ahn: conceptualization, investigation, writing (original draft, review & editing). Deok Ki Cho: conceptualization, investigation, writing (original draft, review & editing). Jin Young Kim: conceptualization, supervision. Ho Won Jang: conceptualization, writing (review & editing), supervision, funding.

Conflicts of interest

There are no conflicts to declare.

Acknowledgements

This work was supported by the National Research Foundation of Korea (NRF) funded by the Korea government Ministry of Science and ICT (MSIT) (2021M3H4A1A03057403, 2021M3D1A2039641). Ho Won Jang acknowledges the KRISS (Korea Research Institute of Standards and Science) MPI Lab. Program. Jin Wook Yang acknowledges the NRF funded by the Korea government MSIT

(RS-2023-00213786). This work was also supported by The Inter-University Semiconductor Research Center and Institute of Engineering Research at Seoul National University provided research facilities for this work.

References

1 Z. Li, S. Fang, H. Sun, R. J. Chung, X. Fang and J. H. He, Solar Hydrogen, *Adv. Energy Mater.*, 2023, **13**, 2203019.
2 P. Chatterjee, M. S. K. Ambati, A. K. Chakraborty, S. Chakrabortty, S. Biring, S. Ramakrishna, T. K. S. Wong, A. Kumar, R. Lawaniya and G. K. Dalapati, Photovoltaic/photo-electrocatalysis integration for green hydrogen: A review, *Energy Convers. Manage.*, 2022, **261**, 115648.
3 W. J. Chang, K. H. Lee, H. Ha, K. Jin, G. Kim, S. T. Hwang, H. M. Lee, S. W. Ahn, W. Yoon, H. Seo, J. S. Hong, Y. K. Go, J. I. Ha and K. T. Nam, Design Principle and Loss Engineering for Photovoltaic-Electrolysis Cell System, *ACS Omega*, 2017, **2**, 1009–1018.
4 J. Y. Kim, J. W. Lee, H. S. Jung, H. Shin and N. G. Park, High-Efficiency Perovskite Solar Cells, *Chem. Rev.*, 2020, **120**, 7867–7918.
5 M. T. Hörantner, T. Leijtens, M. E. Ziffer, G. E. Eperon, M. G. Christoforo, M. D. McGehee and H. J. Snaith, The Potential of Multijunction Perovskite Solar Cells, *ACS Energy Lett.*, 2017, **2**, 2506–2513.
6 Q. Sun, Z. Zhang, T. Zhang, Y. Feng, A. Gu, H. Yu, M. Zhang, X. L. Zhang, J. Zhu, Y. Shen and M. Wang, Integrated 4-Terminal All-Inorganic Perovskite Tandem Solar Cell with Open-Circuit Voltage Exceeding 2.1 v for Water Splitting, *ACS Energy Lett.*, 2022, **7**, 4215–4223.
7 K. Datta, B. Branco, Y. Zhao, V. Zardetto, N. Phung, A. Bracesco, L. Mazzarella, M. M. Wienk, M. Creatore, O. Isabella and R. A. J. Janssen, Efficient Continuous Light-Driven Electrochemical Water Splitting Enabled by Monolithic Perovskite-Silicon Tandem Photovoltaics, *Adv. Mater. Technol.*, 2023, **8**, 2201131.
8 J. Chen, C. Dong, H. Idriss, O. F. Mohammed and O. M. Bakr, Metal Halide Perovskites for Solar-to-Chemical Fuel Conversion, *Adv. Energy Mater.*, 2020, **10**, 1902433.
9 J. H. Kim, Y. K. Kim and J. S. Lee, Perovskite Tandems Advance Solar Hydrogen Production, *Joule*, 2019, **3**, 2892–2894.
10 H. Bian, D. Li, J. Yan and S. F. Liu, Perovskite – A wonder catalyst for solar hydrogen production, *J. Energy Chem.*, 2021, **57**, 325–340.
11 M. G. Lee, J. W. Yang, H. R. Kwon and H. W. Jang, Crystal facet and phase engineering for advanced water splitting, *CrystEngComm*, 2022, **24**, 5838–5864.
12 R. H. Coridan, A. C. Nielander, S. A. Francis, M. T. McDowell, V. Dix, S. M. Chatman and N. S. Lewis, Methods for comparing the performance of energy-conversion systems for use in solar fuels and solar electricity generation, *Energy Environ. Sci.*, 2015, **8**, 2886–2901.
13 M. T. Winkler, C. R. Cox, D. G. Nocera and T. Buonassisi, Modeling integrated photovoltaic-electrochemical devices using steady-state equivalent circuits, *Proc. Natl. Acad. Sci. U. S. A.*, 2013, **110**, E1076–E1082.
14 B. Turan, J. P. Becker, F. Urbain, F. Finger, U. Rau and S. Haas, Upscaling of integrated photoelectrochemical water-splitting devices to large areas, *Nat. Commun.*, 2016, **7**, 12681.
15 G. H. Lin, M. Kapur, R. C. Kainthla and J. O. M. Bockris, One step method to produce hydrogen by a triple stack amorphous silicon solar cell, *Appl. Phys. Lett.*, 1989, **55**, 386–387.
16 E. Verlage, S. Hu, R. Liu, R. J. R. Jones, K. Sun, C. Xiang, N. S. Lewis and H. A. Atwater, A monolithically integrated, intrinsically safe, 10% efficient, solar-driven water-splitting system based on active, stable earth-abundant electrocatalysts in conjunction with tandem III-V light absorbers protected by amorphous TiO_2 films, *Energy Environ. Sci.*, 2015, **8**, 3166–3172.
17 S. Y. Reece, J. A. Hamel, K. Sung, T. D. Jarvi, A. J. Esswein, J. J. H. Pijpers and D. G. Nocera, Wireless Solar Water Splitting Using Silicon-Based Semiconductors and Earth-Abundant Catalysts, *Science*, 2011, **334**, 645–648.
18 J. H. Kim, S. Seo, J. H. Lee, H. Choi, S. Kim, G. Piao, Y. R. Kim, B. Park, J. Lee, Y. Jung, H. Park, S. Lee and K. Lee, Efficient and Stable Perovskite-Based Photocathode for Photoelectrochemical Hydrogen Production, *Adv. Funct. Mater.*, 2021, **31**, 2008277.
19 I. Poli, U. Hintermair, M. Regue, S. Kumar, E. V. Sackville, J. Baker, T. M. Watson, S. Eslava and P. J. Cameron, Graphite-protected $CsPbBr_3$ perovskite photoanodes functionalised with water oxidation catalyst for oxygen evolution in water, *Nat. Commun.*, 2019, **10**, 2079.
20 M. Crespo-Quesada, L. M. Pazos-Outón, J. Warnan, M. F. Kuehnel, R. H. Friend and E. Reisner, Metal-encapsulated organolead halide perovskite photocathode for solar-driven hydrogen evolution in water, *Nat. Commun.*, 2016, **7**, 12555.
21 A. J. Appleby, A. E. Delahoy, S. C. Gau, J. Murphy, M. Kapur and M. Bockris, An amorphous silicon-based one-unit photovoltaic electrolyzer, *Energy*, 1985, **7**, 871–876.
22 Y. Yamada, N. Matsuki, T. Ohmori, H. Mametsuka, M. Kondo, A. Matsuda and E. Suzuki, One chip photovoltaic water electrolysis device, *Int. J. Hydrogen Energy*, 2003, **28**, 1167–1169.
23 N. Kato, S. Mizuno, M. Shiozawa, N. Nojiri, Y. Kawai, K. Fukumoto, T. Morikawa and Y. Takeda, A large-sized cell for solar-driven CO_2 conversion with a solar-to-formate conversion efficiency of 7.2%, *Joule*, 2021, **5**, 687–705.
24 Gurudayal, J. Bullock, D. F. Srankó, C. M. Towle, Y. Lum, M. Hettick, M. C. Scott, A. Javey and J. Ager, Efficient solar-driven electrochemical CO_2 reduction to hydrocarbons and oxygenates, *Energy Environ. Sci.*, 2017, **10**, 2222–2230.

25 F. Urbain, P. Tang, N. M. Carretero, T. Andreu, L. G. Gerling, C. Voz, J. Arbiol and J. R. Morante, A prototype reactor for highly selective solar-driven CO_2 reduction to synthesis gas using nanosized earth-abundant catalysts and silicon photovoltaics, *Energy Environ. Sci.*, 2017, **10**, 2256–2266.
26 J. Luo, J. H. Im, M. T. Mayer, M. Schreier, M. K. Nazeeruddin, N. G. Park, S. D. Tilley, H. J. Fan and M. Grätzel, Water photolysis at 12.3% efficiency via perovskite photovoltaics and Earth-abundant catalysts, *Science*, 2014, **345**, 1593–1596.
27 W. H. Cheng, M. H. Richter, I. Sullivan, D. M. Larson, C. Xiang, B. S. Brunschwig and H. A. Atwater, CO_2 Reduction to CO with 19% Efficiency in a Solar-Driven Gas Diffusion Electrode Flow Cell under Outdoor Solar Illumination, *ACS Energy Lett.*, 2020, **5**, 470–476.
28 C. Battaglia, A. Cuevas and S. De Wolf, High-efficiency crystalline silicon solar cells: Status and perspectives, *Energy Environ. Sci.*, 2016, **9**, 1552–1576.
29 T. Saga, Advances in crystalline silicon solar cell technology for industrial mass production, *NPG Asia Mater.*, 2010, **2**, 96–102.
30 S. Moon, K. Kim, Y. Kim, J. Heo and J. Lee, Highly efficient single-junction GaAs thin-film solar cell on flexible substrate, *Sci. Rep.*, 2016, **6**, 30107.
31 J. S. Mangum, S. Theingi, M. A. Steiner, W. E. McMahon and E. L. Warren, Development of High-Efficiency GaAs Solar Cells Grown on Nanopatterned GaAs Substrates, *Cryst. Growth Des.*, 2021, **21**, 5955–5960.
32 M. Minbashi, A. Ghobadi, E. Yazdani, A. A. Kordbacheh and A. Hajjiah, Efficiency enhancement of CZTSSe solar cells via screening the absorber layer by examining of different possible defects, *Sci. Rep.*, 2020, **10**, 21813.
33 Y. Ji, X. Zhao, Y. Pan, Z. Su, J. Lin, E. M. Akinoglu, Y. Xu, H. Zhang, P. Zhao, Y. Dong, X. Wei, F. Liu and P. Mulvaney, CuSCN Modified Back Contacts for High Performance CZTSSe Solar Cells, *Adv. Funct. Mater.*, 2023, **33**, 2211421.
34 S. Shafian, G. E. Lee, H. Yu, J. H. Jeong and K. Kim, High-Efficiency Vivid Color CIGS Solar Cell Employing Nondestructive Structural Coloration, *Sol. RRL*, 2022, **6**, 2100965.
35 T. S. Lopes, J. P. Teixeira, M. A. Curado, B. R. Ferreira, A. J. N. Oliveira, J. M. V. Cunha, M. Monteiro, A. Violas, J. R. S. Barbosa, P. C. Sousa, I. Çaha, J. Borme, K. Oliveira, J. Ring, W. C. Chen, Y. Zhou, K. Takei, E. Niemi, F. L. Deepak, M. Edoff, G. Brammertz, P. A. Fernandes, B. Vermang and P. M. P. Salomé, $Cu(In,Ga)Se_2$ based ultrathin solar cells the pathway from lab rigid to large scale flexible technology, *npj Flexible Electron.*, 2023, **7**, 4.
36 R. Zhou, Z. Jiang, C. Yang, J. Yu, J. Feng, M. A. Adil, D. Deng, W. Zou, J. Zhang, K. Lu, W. Ma, F. Gao and Z. Wei, All-small-molecule organic solar cells with over 14% efficiency by optimizing hierarchical morphologies, *Nat. Commun.*, 2019, **10**, 5393.
37 F. Liu, L. Zhou, W. Liu, Z. Zhou, Q. Yue, W. Zheng, R. Sun, W. Liu, S. Xu, H. Fan, L. Feng, Y. Yi, W. Zhang and X. Zhu, Organic Solar Cells with 18% Efficiency Enabled by an Alloy Acceptor: A Two-in-One Strategy, *Adv. Mater.*, 2021, **33**, 2100830.
38 Y. Ren, D. Zhang, J. Suo, Y. Cao, F. T. Eickemeyer, N. Vlachopoulos, S. M. Zakeeruddin, A. Hagfeldt and M. Grätzel, Hydroxamic acid pre-adsorption raises the efficiency of cosensitized solar cells, *Nature*, 2023, **613**, 60–65.
39 W. Ghann, H. Kang, T. Sheikh, S. Yadav, T. Chavez-Gil, F. Nesbitt and J. Uddin, Fabrication, Optimization and Characterization of Natural Dye Sensitized Solar Cell, *Sci. Rep.*, 2017, **7**, 41470.
40 S. J. Kim, T. H. Lee, J. M. Yang, J. W. Yang, Y. J. Lee, M. J. Choi, S. A. Lee, J. M. Suh, K. J. Kwak, J. H. Baek, I. H. Im, D. E. Lee, J. Y. Kim, J. Kim, J. S. Han, S. Y. Kim, D. Lee, N. G. Park and H. W. Jang, Vertically aligned two-dimensional halide perovskites for reliably operable artificial synapses, *Mater. Today*, 2022, **52**, 19–30.
41 I. H. Im, S. J. Kim, J. H. Baek, K. J. Kwak, T. H. Lee, J. W. Yang, D. E. Lee, J. Y. Kim, H. R. Kwon, D. Y. Heo, S. Y. Kim and H. W. Jang, Controlling Threshold and Resistive Switch Functionalities in Ag-Incorporated Organometallic Halide Perovskites for Memristive Crossbar Array, *Adv. Funct. Mater.*, 2023, **33**, 2211358.
42 S. Tao, I. Schmidt, G. Brocks, J. Jiang, I. Tranca, K. Meerholz and S. Olthof, Absolute energy level positions in tin- and lead-based halide perovskites, *Nat. Commun.*, 2019, **10**, 2560.
43 I. E. Castelli, J. M. García-Lastra, K. S. Thygesen and K. W. Jacobsen, Bandgap calculations and trends of organometal halide perovskites, *APL Mater.*, 2014, **2**, 081514.
44 D. Kim, H. J. Jung, I. J. Park, B. W. Larson, S. P. Dunfield, C. Xiao, J. Kim, J. Tong, P. Boonmongkolras, S. G. Ji, F. Zhang, S. R. Pae, M. Kim, S. B. Kang, V. Dravid, J. J. Berry, J. Y. Kim, K. Zhu, D. H. Kim and B. Shin, Efficient, stable silicon tandem cells enabled by anion-engineered wide-bandgap perovskites, *Science*, 2020, **368**, 155–160.
45 I. J. Park, J. H. Park, S. G. Ji, M. A. Park, J. H. Jang and J. Y. Kim, A Three-Terminal Monolithic Perovskite/Si Tandem Solar Cell Characterization Platform, *Joule*, 2019, **3**, 807–818.
46 M. Jošt, E. Köhnen, A. Al-Ashouri, T. Bertram, Š. Tomšič, A. Magomedov, E. Kasparavicius, T. Kodalle, B. Lipovšek, V. Getautis, R. Schlatmann, C. A. Kaufmann, S. Albrecht and M. Topič, Perovskite/CIGS Tandem Solar Cells: From Certified 24.2% toward 30% and beyond, *ACS Energy Lett.*, 2022, **7**, 1298–1307.
47 T. J. Jacobsson, A. Hultqvist, S. Svanström, L. Riekehr, U. B. Cappel, E. Unger, H. Rensmo, E. M. J. Johansson, M. Edoff and G. Boschloo, 2-Terminal CIGS-perovskite tandem cells: A layer by layer exploration, *Sol. Energy*, 2020, **207**, 270–288.
48 M. Moradbeigi and M. Razaghi, Investigation of optical and electrical properties of novel 4T all perovskite tandem solar cell, *Sci. Rep.*, 2022, **12**, 6733.

49 M. A. Shafi, L. Khan, S. Ullah, M. Y. Shafi, A. Bouich, H. Ullah and B. Mari, Novel compositional engineering for ~26% efficient CZTS-perovskite tandem solar cell, *Optik*, 2022, **253**, 168568.
50 W. Chen, Y. Zhu, J. Xiu, G. Chen, H. Liang, S. Liu, H. Xue, E. Birgersson, J. W. Ho, X. Qin, J. Lin, R. Ma, T. Liu, Y. He, A. M. C. Ng, X. Guo, Z. He, H. Yan, A. B. Djurišić and Y. Hou, Monolithic perovskite/organic tandem solar cells with 23.6% efficiency enabled by reduced voltage losses and optimized interconnecting layer, *Nat. Energy*, 2022, **7**, 229–237.
51 K. O. Brinkmann, T. Becker, F. Zimmermann, C. Kreusel, T. Gahlmann, M. Theisen, T. Haeger, S. Olthof, C. Tückmantel, M. Günster, T. Maschwitz, F. Göbelsmann, C. Koch, D. Hertel, P. Caprioglio, F. Peña-Camargo, L. Perdigón-Toro, A. Al-Ashouri, L. Merten, A. Hinderhofer, L. Gomell, S. Zhang, F. Schreiber, S. Albrecht, K. Meerholz, D. Neher, M. Stolterfoht and T. Riedl, Perovskite–organic tandem solar cells with indium oxide interconnect, *Nature*, 2022, **604**, 280–286.
52 J. Zheng, G. Wang, W. Duan, M. A. Mahmud, H. Yi, C. Xu, A. Lambertz, S. Bremner, K. Ding, S. Huang and A. W. Y. Ho-Baillie, Monolithic Perovskite-Perovskite-Silicon Triple-Junction Tandem Solar Cell with an Efficiency of over 20%, *ACS Energy Lett.*, 2022, **7**, 3003–3005.
53 Q. Jiang, J. Tong, R. A. Scheidt, X. Wang, A. E. Louks, Y. Xian, R. Tirawat, A. F. Palmstrom, M. P. Hautzinger, S. P. Harvey, S. Johnston, L. T. Schelhas, B. W. Larson, E. L. Warren, M. C. Beard, J. J. Berry, Y. Yan and K. Zhu, Compositional texture engineering for highly stable wide-bandgap perovskite solar cells, *Science*, 2022, **378**, 1295–1300.
54 A. Al-Ashouri, E. Köhnen, B. Li, A. Magomedov, H. Hempel, P. Caprioglio, J. A. Márquez, A. Belen, M. Vilches, E. Kasparavicius, J. A. Smith, N. Phung, D. Menzel, M. Grischek, L. Kegelmann, D. Skroblin, C. Gollwitzer, T. Malinauskas, M. Jošt, G. Matič, B. Rech, R. Schlatmann, M. Topič, L. Korte, A. Abate, B. Stannowski, D. Neher, M. Stolterfoht, T. Unold, V. Getautis and S. Albrecht, Monolithic perovskite/silicon tandem solar cell with >29% efficiency by enhanced hole extraction, *Science*, 2020, **370**, 1300–1309.
55 J. Jeong, M. Kim, J. Seo, H. Lu, P. Ahlawat, A. Mishra, Y. Yang, M. A. Hope, F. T. Eickemeyer, M. Kim, Y. J. Yoon, I. W. Choi, B. P. Darwich, S. J. Choi, Y. Jo, J. H. Lee, B. Walker, S. M. Zakeeruddin, L. Emsley, U. Rothlisberger, A. Hagfeldt, D. S. Kim, M. Grätzel and J. Y. Kim, Pseudo-halide anion engineering for α-FAPbI3 perovskite solar cells, *Nature*, 2021, **592**, 381–385.
56 K. Xiao, J. Wen, Q. Han, R. Lin, Y. Gao, S. Gu, Y. Zang, Y. Nie, J. Zhu, J. Xu and H. Tan, Solution-processed monolithic all-perovskite triple-junction solar cells with efficiency exceeding 20%, *ACS Energy Lett.*, 2020, **5**, 2819–2826.
57 Y. Jiao, Y. Zheng, M. Jaroniec and S. Z. Qiao, Design of electrocatalysts for oxygen- and hydrogen-involving energy conversion reactions, *Chem. Soc. Rev.*, 2015, **44**, 2060–2086.
58 I. C. Man, H. Y. Su, F. Calle-Vallejo, H. A. Hansen, J. I. Martínez, N. G. Inoglu, J. Kitchin, T. F. Jaramillo, J. K. Nørskov and J. Rossmeisl, Universality in Oxygen Evolution Electrocatalysis on Oxide Surfaces, *ChemCatChem*, 2011, **3**, 1159–1165.
59 S. Li, X. Zhou, G. Fang, G. Xie, X. Liu, X. Lin and H. J. Qiu, Multicomponent Spinel Metal Oxide Nanocomposites as High-Performance Bifunctional Catalysts in Zn-Air Batteries, *ACS Appl. Energy Mater.*, 2020, **3**, 7710–7718.
60 J. Sun, N. Guo, Z. Shao, K. Huang, Y. Li, F. He and Q. Wang, A Facile Strategy to Construct Amorphous Spinel-Based Electrocatalysts with Massive Oxygen Vacancies Using Ionic Liquid Dopant, *Adv. Energy Mater.*, 2018, **8**, 1800980.
61 X. Han, C. Yu, S. Zhou, C. Zhao, H. Huang, J. Yang, Z. Liu, J. Zhao and J. Qiu, Ultrasensitive Iron-Triggered Nanosized Fe–CoOOH Integrated with Graphene for Highly Efficient Oxygen Evolution, *Adv. Energy Mater.*, 2017, **7**, 1602148.
62 M. Gong, Y. Li, H. Wang, Y. Liang, J. Z. Wu, J. Zhou, J. Wang, T. Regier, F. Wei and H. Dai, An advanced Ni-Fe layered double hydroxide electrocatalyst for water oxidation, *J. Am. Chem. Soc.*, 2013, **135**, 8452–8455.
63 L. Yang, L. Xie, X. Ren, Z. Wang, Z. Liu, G. Du, A. M. Asiri, Y. Yao and X. Sun, Hierarchical $CuCo_2S_4$ nanoarrays for high-efficient and durable water oxidation electrocatalysis, *Chem. Commun.*, 2017, **54**, 78–81.
64 J. Jiang, S. Lu, W. K. Wang, G. X. Huang, B. C. Huang, F. Zhang, Y. J. Zhang and H. Q. Yu, Ultrahigh electrocatalytic oxygen evolution by iron-nickel sulfide nanosheets/reduced graphene oxide nanohybrids with an optimized autoxidation process, *Nano Energy*, 2018, **43**, 300–309.
65 P. He, X.-Y. Yu and X. W. D. Lou, Carbon-Incorporated Nickel-Cobalt Mixed Metal Phosphide Nanoboxes with Enhanced Electrocatalytic Activity for Oxygen Evolution, *Angew. Chem.*, 2017, **129**, 3955–3958.
66 R. Wu, B. Xiao, Q. Gao, Y. Zheng, X. Zheng, J. Zhu, M. Gao and S. Yu, A Janus Nickel Cobalt Phosphide Catalyst for High–Efficiency Neutral–pH Water Splitting, *Angew. Chem.*, 2018, **130**, 15671–15675.
67 Q. Wang, Z. Zhang, C. Cai, M. Wang, Z. L. Zhao, M. Li, X. Huang, S. Han, H. Zhou, Z. Feng, L. Li, J. Li, H. Xu, J. S. Francisco and M. Gu, Single Iridium Atom Doped Ni_2P Catalyst for Optimal Oxygen Evolution, *J. Am. Chem. Soc.*, 2021, **143**, 13605–13615.
68 P. Li, M. Wang, X. Duan, L. Zheng, X. Cheng, Y. Zhang, Y. Kuang, Y. Li, Q. Ma, Z. Feng, W. Liu and X. Sun, Boosting oxygen evolution of single-atomic ruthenium through electronic coupling with cobalt-iron layered double hydroxides, *Nat. Commun.*, 2019, **10**, 1711.
69 X. Zheng, J. Tang, A. Gallo, J. A. G. Torres, X. Yu, C. J. Athanitis, E. M. Been, P. Ercius, H. Mao, S. C. Fakra, C. Song, R. C. Davis, J. A. Reimer, J. Vinson, M. Bajdich

and Y. Cui, Origin of enhanced water oxidation activity in an iridium single atom anchored on NiFe oxyhydroxide catalyst, *Proc. Natl. Acad. Sci. U. S. A.*, 2021, **118**, e2101817118.

70 A. Peugeot, C. E. Creissen, D. Karapinar, H. N. Tran, M. Schreiber and M. Fontecave, Benchmarking of oxygen evolution catalysts on porous nickel supports, *Joule*, 2021, **5**, 1281–1300.

71 T. R. Cook, D. K. Dogutan, S. Y. Reece, Y. Surendranath, T. S. Teets and D. G. Nocera, Solar energy supply and storage for the legacy and nonlegacy worlds, *Chem. Rev.*, 2010, **110**, 6474–6502.

72 S. Anantharaj and V. Aravindan, Developments and Perspectives in 3d Transition-Metal-Based Electrocatalysts for Neutral and Near-Neutral Water Electrolysis, *Adv. Energy Mater.*, 2020, **10**, 1902666.

73 Y. Duan, Z. Yu, S. Hu, X. Zheng, C. Zhang, H. Ding, B. Hu, Q. Fu, Z. Yu, X. Zheng, J. Zhu, M. Gao and S. Yu, Scaled–Up Synthesis of Amorphous NiFeMo Oxides and Their Rapid Surface Reconstruction for Superior Oxygen Evolution Catalysis, *Angew. Chem.*, 2019, **131**, 15919–15924.

74 X. Li, L. Liu, X. Ren, J. Gao, Y. Huang and B. Liu, Microenvironment modulation of single-atom catalysts and their roles in electrochemical energy conversion, *Sci. Adv.*, 2020, **6**, eabb6833.

75 X. Wang, L. Sun, W. Zhou, L. Yang, G. Ren, H. Wu and W. Q. Deng, Iron single-atom catalysts confined in covalent organic frameworks for efficient oxygen evolution reaction, *Cell Rep. Phys. Sci.*, 2022, **3**, 100804.

76 S. Liang, L. Huang, Y. Gao, Q. Wang and B. Liu, Electrochemical Reduction of CO_2 to CO over Transition Metal/N-Doped Carbon Catalysts: The Active Sites and Reaction Mechanism, *Adv. Sci.*, 2021, **8**, 2102886.

77 S. Zhao, S. Li, T. Guo, S. Zhang, J. Wang, Y. Wu and Y. Chen, Advances in Sn-Based Catalysts for Electrochemical CO_2 Reduction, *Nano-Micro Lett.*, 2019, **11**, 62.

78 J. T. Feaster, C. Shi, E. R. Cave, T. Hatsukade, D. N. Abram, K. P. Kuhl, C. Hahn, J. K. Nørskov and T. F. Jaramillo, Understanding Selectivity for the Electrochemical Reduction of Carbon Dioxide to Formic Acid and Carbon Monoxide on Metal Electrodes, *ACS Catal.*, 2017, **7**, 4822–4827.

79 Y. Hori, A. Murata and R. Takahashi, Formation of Hydrocarbons in the Electrochemical Reduction of Carbon Dioxide at a Copper Electrode in Aqueous Solution, *J. Chem. Soc., Faraday Trans.*, 1989, **85**, 2309–2326.

80 A. Bagger, W. Ju, A. S. Varela, P. Strasser and J. Rossmeisl, Electrochemical CO2 Reduction: A Classification Problem, *ChemPhysChem*, 2017, **18**, 3266–3273.

81 Q. Lin, A. Armin, R. C. R. Nagiri, P. L. Burn and P. Meredith, Electro-optics of perovskite solar cells, *Nat. Photonics*, 2015, **9**, 106–112.

82 D. P. Mcmeekin, G. Sadoughi, W. Rehman, G. E. Eperon, M. Saliba, M. T. Hörantner, A. Haghighirad, N. Sakai, L. Korte, B. Rech, M. B. Johnston, L. M. Herz and H. J. Snaith, A mixed-cation lead mixed-halide perovskite absorber for tandem solar cells, *Science*, 2016, **351**, 151–155.

83 G. E. Eperon, S. D. Stranks, C. Menelaou, M. B. Johnston, L. M. Herz and H. J. Snaith, Formamidinium lead trihalide: A broadly tunable perovskite for efficient planar heterojunction solar cells, *Energy Environ. Sci.*, 2014, **7**, 982–988.

84 F. Hao, C. C. Stoumpos, R. P. H. Chang and M. G. Kanatzidis, Anomalous band gap behavior in mixed Sn and Pb perovskites enables broadening of absorption spectrum in solar cells, *J. Am. Chem. Soc.*, 2014, **136**, 8094–8099.

85 Z. Li, T. R. Klein, D. H. Kim, M. Yang, J. J. Berry, M. F. A. M. Van Hest and K. Zhu, Scalable fabrication of perovskite solar cells, *Nat. Rev. Mater.*, 2018, **3**, 18017.

86 Y. Deng, X. Zheng, Y. Bai, Q. Wang, J. Zhao and J. Huang, Surfactant-controlled ink drying enables high-speed deposition of perovskite films for efficient photovoltaic modules, *Nat. Energy*, 2018, **3**, 560–566.

87 A. Kojima, K. Teshima, Y. Shirai and T. Miyasaka, Organometal halide perovskites as visible-light sensitizers for photovoltaic cells, *J. Am. Chem. Soc.*, 2009, **131**, 6050–6051.

88 Q. Q. Chu, B. Ding, J. Peng, H. Shen, X. Li, Y. Liu, C. X. Li, C. J. Li, G. J. Yang, T. P. White and K. R. Catchpole, Highly stable carbon-based perovskite solar cell with a record efficiency of over 18% via hole transport engineering, *J. Mater. Sci. Technol.*, 2019, **35**, 987–993.

89 J. Cheng, I. Choi, W. Kim, H. Li, B. Koo and M. J. Ko, Wide-band-gap (2.0 eV) perovskite solar cells with a V_{oc} of 1.325 V fabricated by a green-solvent strategy, *ACS Appl. Mater. Interfaces*, 2023, **15**, 23077–23084.

90 W. Shockley and H. J. Queisser, Detailed balance limit of efficiency of p-n junction solar cells, *J. Appl. Phys.*, 1961, **32**, 510–519.

91 M. A. Green, E. D. Dunlop, G. Siefer, M. Yoshita, N. Kopidakis, K. Bothe and X. Hao, Solar cell efficiency tables (Version 61), *Prog. Photovoltaics Res. Appl.*, 2023, **31**, 3–16.

92 G. E. Eperon, M. T. Hörantner and H. J. Snaith, Metal halide perovskite tandem and multiple-junction photovoltaics, *Nat. Rev. Chem.*, 2017, **1**, 0095.

93 C. Li, Y. Wang and W. C. H. Choy, Efficient Interconnection in Perovskite Tandem Solar Cells, *Small Methods*, 2020, **4**, 2000093.

94 M. Zhang and Z. Lin, Efficient interconnecting layers in monolithic all-perovskite tandem solar cells, *Energy Environ. Sci.*, 2022, **15**, 3152–3170.

95 J. Werner, C. H. Weng, A. Walter, L. Fesquet, J. P. Seif, S. De Wolf, B. Niesen and C. Ballif, Efficient Monolithic Perovskite/Silicon Tandem Solar Cell with Cell Area >1 cm^2, *J. Phys. Chem. Lett.*, 2016, **7**, 161–166.

96 Z. Yu, Z. Yang, Z. Ni, Y. Shao, B. Chen, Y. Lin, H. Wei, Z. J. Yu, Z. Holman and J. Huang, Simplified interconnec-

tion structure based on C60/SnO2-x for all-perovskite tandem solar cells, *Nat. Energy*, 2020, **5**, 657–665.

97 D. Zhao, C. Chen, C. Wang, M. M. Junda, Z. Song, C. R. Grice, Y. Yu, C. Li, B. Subedi, N. J. Podraza, X. Zhao, G. Fang, R. G. Xiong, K. Zhu and Y. Yan, Efficient two-terminal all-perovskite tandem solar cells enabled by high-quality low-bandgap absorber layers, *Nat. Energy*, 2018, **3**, 1093–1100.

98 M. Jošt, L. Kegelmann, L. Korte and S. Albrecht, Monolithic Perovskite Tandem Solar Cells: A Review of the Present Status and Advanced Characterization Methods Toward 30% Efficiency, *Adv. Energy Mater.*, 2020, **10**, 1904102.

99 A. Alasfour, Z. J. Yu, W. Weigand, D. Quispe and Z. C. Holman, Sub-micrometer random-pyramid texturing of silicon solar wafers with excellent surface passivation and low reflectance, *Sol. Energy Mater. Sol. Cells*, 2020, **218**, 110761.

100 J. Werner, L. Barraud, A. Walter, M. Bräuninger, F. Sahli, D. Sacchetto, N. Tétreault, B. Paviet-Salomon, S. J. Moon, C. Allebé, M. Despeisse, S. Nicolay, S. De Wolf, B. Niesen and C. Ballif, Efficient Near-Infrared-Transparent Perovskite Solar Cells Enabling Direct Comparison of 4-Terminal and Monolithic Perovskite/Silicon Tandem Cells, *ACS Energy Lett.*, 2016, **1**, 474–480.

101 F. Sahli, J. Werner, B. A. Kamino, M. Bräuninger, R. Monnard, B. Paviet-Salomon, L. Barraud, L. Ding, J. J. D. Leon, D. Sacchetto, G. Cattaneo, M. Despeisse, M. Boccard, S. Nicolay, Q. Jeangros, B. Niesen and C. Ballif, Fully textured monolithic perovskite/silicon tandem solar cells with 25.2% power conversion efficiency, *Nat. Mater.*, 2018, **17**, 820–826.

102 B. Chen, Z. J. Yu, S. Manzoor, S. Wang, W. Weigand, Z. Yu, G. Yang, Z. Ni, X. Dai, Z. C. Holman and J. Huang, Blade-Coated Perovskites on Textured Silicon for 26%-Efficient Monolithic Perovskite/Silicon Tandem Solar Cells, *Joule*, 2020, **4**, 850–864.

103 D. J. Slotcavage, H. I. Karunadasa and M. D. McGehee, Light-Induced Phase Segregation in Halide-Perovskite Absorbers, *ACS Energy Lett.*, 2016, **1**, 1199–1205.

104 E. T. Hoke, D. J. Slotcavage, E. R. Dohner, A. R. Bowring, H. I. Karunadasa and M. D. McGehee, Reversible photo-induced trap formation in mixed-halide hybrid perovskites for photovoltaics, *Chem. Sci.*, 2015, **6**, 613–617.

105 G. Yang, Z. Ni, Z. J. Yu, B. W. Larson, Z. Yu, B. Chen, A. Alasfour, X. Xiao, J. M. Luther, Z. C. Holman and J. Huang, Defect engineering in wide-bandgap perovskites for efficient perovskite–silicon tandem solar cells, *Nat. Photonics*, 2022, **16**, 588–594.

106 X. Luo, H. Luo, H. Li, R. Xia, X. Zheng, Z. Huang, Z. Liu, H. Gao, X. Zhang, S. Li, Z. Feng, Y. Chen and H. Tan, Efficient Perovskite/Silicon Tandem Solar Cells on Industrially Compatible Textured Silicon, *Adv. Mater.*, 2023, **35**, 2207883.

107 P. Tockhorn, J. Sutter, A. Cruz, P. Wagner, K. Jäger, D. Yoo, F. Lang, M. Grischek, B. Li, J. Li, O. Shargaieva, E. Unger, A. Al-Ashouri, E. Köhnen, M. Stolterfoht, D. Neher, R. Schlatmann, B. Rech, B. Stannowski, S. Albrecht and C. Becker, Nano-optical designs for high-efficiency monolithic perovskite–silicon tandem solar cells, *Nat. Nanotechnol.*, 2022, **17**, 1214–1221.

108 J. Zheng, W. Duan, Y. Guo, Z. C. Zhao, H. Yi, F. J. Ma, L. G. Caro, C. Yi, J. Bing, S. Tang, J. Qu, K. C. Fong, X. Cui, Y. Zhu, L. Yang, A. Lambertz, M. A. Mahmud, H. Chen, C. Liao, G. Wang, M. Jankovec, C. Xu, A. Uddin, J. M. Cairney, S. Bremner, S. Huang, K. Ding, D. R. McKenzie and A. W. Y. Ho-Baillie, Efficient monolithic perovskite-Si tandem solar cells enabled by an ultra-thin indium tin oxide interlayer, *Energy Environ. Sci.*, 2023, **16**, 1223–1233.

109 C. Liang, H. Gu, Y. Xia, Z. Wang, X. Liu, J. Xia, S. Zuo, Y. Hu, X. Gao, W. Hui, L. Chao, T. Niu, M. Fang, H. Lu, H. Dong, H. Yu, S. Chen, X. Ran, L. Song, B. Li, J. Zhang, Y. Peng, G. Shao, J. Wang, Y. Chen, G. Xing and W. Huang, Two-dimensional Ruddlesden–Popper layered perovskite solar cells based on phase-pure thin films, *Nat. Energy*, 2021, **6**, 38–45.

110 Y. Choi, D. Koo, G. Jeong, U. Kim, H. Kim, F. Huang and H. Park, A vertically oriented two-dimensional Ruddlesden–Popper phase perovskite passivation layer for efficient and stable inverted perovskite solar cells, *Energy Environ. Sci.*, 2022, **15**, 3369–3378.

111 S. Wang, P. Wang, B. Shi, C. Sun, H. Sun, S. Qi, Q. Huang, S. Xu, Y. Zhao and X. Zhang, Inorganic Perovskite Surface Reconfiguration for Stable Inverted Solar cell with 20.38% Efficiency and its Application in Tandem Devices, *Adv. Mater.*, 2023, 2300581.

112 J. C. Blancon, J. Even, C. C. Stoumpos, M. G. Kanatzidis and A. D. Mohite, Semiconductor physics of organic-inorganic 2D halide perovskites, *Nat. Nanotechnol.*, 2020, **15**, 969–985.

113 J. Song, H. Xie, E. L. Lim, A. Hagfeldt and D. Bi, Progress and perspective on inorganic $CsPbI_2Br$ perovskite solar cells, *Adv. Energy Mater.*, 2022, **12**, 2201854.

114 J. Wang, V. Zardetto, K. Datta, D. Zhang, M. M. Wienk and R. A. J. Janssen, 16.8% Monolithic all-perovskite triple-junction solar cells via a universal two-step solution process, *Nat. Commun.*, 2020, **11**, 5254.

115 D. P. McMeekin, S. Mahesh, N. K. Noel, M. T. Klug, J. C. Lim, J. H. Warby, J. M. Ball, L. M. Herz, M. B. Johnston and H. J. Snaith, Solution-Processed All-Perovskite Multi-junction Solar Cells, *Joule*, 2019, **3**, 387–401.

116 A. De Vos, Detailed balance limit of the efficiency of tandem solar cells, *J. Phys. D: Appl. Phys.*, 1980, **13**, 839–846.

117 T. Duong, H. K. Mulmudi, Y. Wu, X. Fu, H. Shen, J. Peng, N. Wu, H. T. Nguyen, D. Macdonald, M. Lockrey, T. P. White, K. Weber and K. Catchpole, Light and Electrically Induced Phase Segregation and Its Impact on the Stability of Quadruple Cation High Bandgap Perovskite Solar Cells, *ACS Appl. Mater. Interfaces*, 2017, **9**, 26859–26866.

118 J. Wen, Y. Zhao, Z. Liu, H. Gao, R. Lin, S. Wan, C. Ji, K. Xiao, Y. Gao, Y. Tian, J. Xie, C. J. Brabec and H. Tan, Steric Engineering Enables Efficient and Photostable Wide-Bandgap Perovskites for All-Perovskite Tandem Solar Cells, *Adv. Mater.*, 2022, **34**, 2110356.

119 Z. Wang, L. Zeng, T. Zhu, H. Chen, B. Chen, D. J. Kubicki, A. Balvanz, C. Li, A. Maxwell, E. Ugur, R. dos Reis, M. Cheng, G. Yang, B. Subedi, D. Luo, J. Hu, J. Wang, S. Teale, S. Mahesh, S. Wang, S. Hu, E. Jung, M. Wei, S. M. Park, L. Grater, E. Aydin, Z. Song, N. J. Podraza, Z.-H. Lu, J. Huang, V. P. Dravid, S. De Wolf, Y. Yan, M. Grätzel, M. Kanatzidis and E. Sargent, Suppressed phase segregation for triple-junction perovskite solar cells, *Nature*, 2023, **618**, 74–79.

120 Y. Takahashi, R. Obara, Z. Z. Lin, Y. Takahashi, T. Naito, T. Inabe, S. Ishibashi and K. Terakura, Charge-transport in tin-iodide perovskite $CH_3NH_3SnI_3$: Origin of high conductivity, *Dalton Trans.*, 2011, **40**, 5563–5568.

121 J. Tong, Z. Song, D. H. Kim, X. Chen, C. Chen, A. F. Palmstrom, P. F. Ndione, M. O. Reese, S. P. Dunfield, O. G. Reid, J. Liu, F. Zhang, S. P. Harvey, Z. Li, S. T. Christensen, G. Teeter, D. Zhao, M. M. Al-Jassim, M. F. A. M. van Hest, M. C. Beard, S. E. Shaheen, J. J. Berry, Y. Yan and K. Zhu, Carrier lifetimes of >1 ms in Sn-Pb perovskites enable efficient all-perovskite tandem solar cells, *Science*, 2019, **364**, 475–479.

122 R. Lin, K. Xiao, Z. Qin, Q. Han, C. Zhang, M. Wei, M. I. Saidaminov, Y. Gao, J. Xu, M. Xiao, A. Li, J. Zhu, E. H. Sargent and H. Tan, Monolithic all-perovskite tandem solar cells with 24.8% efficiency exploiting comproportionation to suppress Sn(ii) oxidation in precursor ink, *Nat. Energy*, 2019, **4**, 864–873.

123 K. Xiao, R. Lin, Q. Han, Y. Hou, Z. Qin, H. T. Nguyen, J. Wen, M. Wei, V. Yeddu, M. I. Saidaminov, Y. Gao, X. Luo, Y. Wang, H. Gao, C. Zhang, J. Xu, J. Zhu, E. H. Sargent and H. Tan, All-perovskite tandem solar cells with 24.2% certified efficiency and area over 1 cm^2 using surface-anchoring zwitterionic antioxidant, *Nat. Energy*, 2020, **5**, 870–880.

124 R. Lin, J. Xu, M. Wei, Y. Wang, Z. Qin, Z. Liu, J. Wu, K. Xiao, B. Chen, S. M. Park, G. Chen, H. R. Atapattu, K. R. Graham, J. Xu, J. Zhu, L. Li, C. Zhang, E. H. Sargent and H. Tan, All-perovskite tandem solar cells with improved grain surface passivation, *Nature*, 2022, **603**, 73–78.

125 J. Tong, Q. Jiang, A. J. Ferguson, A. F. Palmstrom, X. Wang, J. Hao, S. P. Dunfield, A. E. Louks, S. P. Harvey, C. Li, H. Lu, R. M. France, S. A. Johnson, F. Zhang, M. Yang, J. F. Geisz, M. D. McGehee, M. C. Beard, Y. Yan, D. Kuciauskas, J. J. Berry and K. Zhu, Carrier control in Sn–Pb perovskites via 2D cation engineering for all-perovskite tandem solar cells with improved efficiency and stability, *Nat. Energy*, 2022, **7**, 642–651.

126 J. Luo, R. He, H. Lai, C. Chen, J. Zhu, Y. Xu, F. Yao, T. Ma, Y. Luo, Z. Yi, Y. Jiang, Z. Gao, J. Wang, W. Wang, H. Huang, Y. Wang, S. Ren, Q. Lin, C. Wang, F. Fu and D. Zhao, Improved Carrier Management Via a Multifunctional Modifier for High–Quality Low–Bandgap Sn–Pb Perovskites and Efficient All–Perovskite Tandem Solar Cells, *Adv. Mater.*, 2023, 2300352.

127 B. Chen, P. N. Rudd, S. Yang, Y. Yuan and J. Huang, Imperfections and their passivation in halide perovskite solar cells, *Chem. Soc. Rev.*, 2019, **48**, 3842–3867.

128 N. K. Noel, A. Abate, S. D. Stranks, E. S. Parrott, V. M. Burlakov, A. Goriely and H. J. Snaith, Enhanced photoluminescence and solar cell performance via Lewis base passivation of organic-inorganic lead halide perovskites, *ACS Nano*, 2014, **8**, 9815–9821.

129 C. Wang, Y. Zhao, T. Ma, Y. An, R. He, J. Zhu, C. Chen, S. Ren, F. Fu, D. Zhao and X. Li, A universal close-space annealing strategy towards high-quality perovskite absorbers enabling efficient all-perovskite tandem solar cells, *Nat. Energy*, 2022, **7**, 744–753.

130 M. Yang, Z. Li, M. O. Reese, O. G. Reid, D. H. Kim, S. Siol, T. R. Klein, Y. Yan, J. J. Berry, M. F. A. M. Van Hest and K. Zhu, Perovskite ink with wide processing window for scalable high-efficiency solar cells, *Nat. Energy*, 2017, **2**, 17038.

131 Z. Yang, W. Zhang, S. Wu, H. Zhu, Z. Liu, Z. Liu, Z. Jiang, R. Chen, J. Zhou, Q. Lu, Z. Xiao, L. Shi, H. Chen, L. K. Ono, S. Zhang, Y. Zhang, Y. Qi, L. Han and W. Chen, *Sci. Adv.*, 2021, **7**, eabg3749.

132 J. B. Whitaker, D. H. Kim, B. W. Larson, F. Zhang, J. J. Berry, M. F. A. M. Van Hest and K. Zhu, Scalable slot-die coating of high performance perovskite solar cells, *Sustainable Energy Fuels*, 2018, **2**, 2442–2449.

133 J. E. Bishop, J. A. Smith and D. G. Lidzey, Development of Spray-Coated Perovskite Solar Cells, *ACS Appl. Mater. Interfaces*, 2020, **12**, 48237–48245.

134 X. Peng, J. Yuan, S. Shen, M. Gao, A. S. R. Chesman, H. Yin, J. Cheng, Q. Zhang and D. Angmo, *Adv. Funct. Mater.*, 2017, **27**, 1703404.

135 K. Xiao, Y.-H. Lin, M. Zhang, R. D. J. Oliver, X. Wang, Z. Liu, X. Luo, J. Li, D. Lai, H. Luo, R. Lin, J. Xu, Y. Hou, H. J. Snaith and H. Tan, Scalable processing for realizing 21.7%-efficient all-perovskite tandem solar modules, *Science*, 2022, **376**, 762–767.

136 R. He, W. Wang, Z. Yi, F. Lang, C. Chen, J. Luo, J. Zhu, J. Thiesbrummel, S. Shah, K. Wei, Y. Luo, C. Wang, H. Lai, H. Huang, J. Zhou, B. Zou, X. Yin, S. Ren, X. Hao, L. Wu, J. Zhang, J. Zhang, M. Stolterfoht, F. Fu, W. Tang and D. Zhao, All-perovskite tandem 1 cm^2 cells with improved interface quality, *Nature*, 2023, **618**, 80–86.

137 H. Zhao and Z. Yuan, Process and Perspectives for Solar-Driven Water Electrolysis to Produce Green Hydrogen, *Adv. Energy Mater.*, 2023, **13**, 2300254.

138 A. Kumar, M. Mucalo, L. Bolzoni, Y. Li, Y. Qu and F. Yang, Facile synthesis of a NiMnFeCrCu high entropy alloy for electrocatalytic oxygen evolution reactions, *Mater. Today Sustainable*, 2023, **22**, 100360.

139 B. Zhang, L. Wang, Z. Cao, S. M. Kozlov, F. P. G. Arquer, C. T. Dinh, J. Li, Z. Wang, X. Zheng, L. Zhang, Y. Wen,

O. Voznyy, R. Comin, P. De Luna, T. Regier, W. Bi, E. E. Alp, C. W. Pao, L. Zheng, Y. Hu, Y. Ji, Y. Li, Y. Zhang, L. Cavallo, H. Peng and E. H. Sargent, High-valence metals improve oxygen evolution reaction performance by modulating 3d metal oxidation cycle energetics, *Nat. Catal.*, 2020, **3**, 985–992.

140 E. Detsi, J. B. Cook, B. K. Lesel, C. L. Turner, Y. L. Liang, S. Robbennolt and S. H. Tolbert, Mesoporous $Ni_{60}Fe_{30}Mn_{10}$-alloy based metal/metal oxide composite thick films as highly active and robust oxygen evolution catalysts, *Energy Environ. Sci.*, 2016, **9**, 540–549.

141 Y. H. Jo, S. Jung, W. M. Choi, S. S. Sohn, H. S. Kim, B. J. Lee, N. J. Kim and S. Lee, Cryogenic strength improvement by utilizing room-temperature deformation twinning in a partially recrystallized VCrMnFeCoNi high-entropy alloy, *Nat. Commun.*, 2017, **8**, 15719.

142 L. Gao, J. Song, Z. Jiao, W. Liao, J. Luan, J. U. Surjadi, J. Li, H. Zhang, D. Sun, C. T. Liu and Y. Lu, High-Entropy Alloy (HEA)-Coated Nanolattice Structures and Their Mechanical Properties, *Adv. Eng. Mater.*, 2018, **20**, 1700625.

143 T. Löffler, A. Savan, A. Garzón-Manjón, M. Meischein, C. Scheu, A. Ludwig and W. Schuhmann, Toward a Paradigm Shift in Electrocatalysis Using Complex Solid Solution Nanoparticles, *ACS Energy Lett.*, 2019, **4**, 1206–1214.

144 H. Park, J. W. Bae, T. H. Lee, I. J. Park, C. Kim, M. G. Lee, S. A. Lee, J. W. Yang, M. J. Choi, S. H. Hong, S. Y. Kim, S. H. Ahn, J. Y. Kim, H. S. Kim and H. W. Jang, Surface-Tailored Medium Entropy Alloys as Radically Low Overpotential Oxygen Evolution Electrocatalysts, *Small*, 2022, **8**, 2105611.

145 S. A. Lee, J. W. Yang, S. Choi and H. W. Jang, Nanoscale electrodeposition: Dimension control and 3D conformality, *Exploration*, 2021, **1**, 20210012.

146 W. Ye, T. W. Kim and D. H. Park, Layered double hydroxide nanomaterials for bifunctional ORR/OER electro-catalyst, *J. Korean Ceram. Soc.*, 2022, **59**, 763–774.

147 Z. Li, S. Wu, J. Zhang, K. C. Lee, H. Lei, F. Lin, Z. Wang, Z. Zhu and A. K. Y. Jen, Hybrid Perovskite-Organic Flexible Tandem Solar Cell Enabling Highly Efficient Electrocatalysis Overall Water Splitting, *Adv. Energy Mater.*, 2020, **10**, 2000361.

148 M. K. Lee, M. Shokouhimehr, S. Y. Kim and H. W. Jang, Two-Dimensional Metal–Organic Frameworks and Covalent–Organic Frameworks for Electrocatalysis: Distinct Merits by the Reduced Dimension, *Adv. Energy Mater.*, 2022, **12**, 2003990.

149 M. K. Lee, S. Choi, H. Park, T. H. Lee, S. A. Lee, J. W. Yang, S. G. Ji, W. S. Cheon, S. H. Ahn, S. Y. Kim, M. Shokouhimehr, J. Y. Kim and H. W. Jang, 2D Ni–Naphthalene–2,6–Dicarboxylic Acid Metal–Organic Framework as Electrocatalysts for Efficient Overall Water Splitting, *Energy Technol.*, 2023, 2201203.

150 S. Pan, R. Li, Q. Zhang, C. Cui, M. Wang, B. Shi, P. Wang, C. Zhang, B. Zhang, Y. Zhao and X. Zhang, An over 20% solar-to-hydrogen efficiency system comprising a self-reconstructed NiCoFe-based hydroxide nanosheet electrocatalyst and monolithic perovskite/silicon tandem solar cell, *J. Mater. Chem. A*, 2021, **9**, 14085–14092.

151 J. Park, T. H. Lee, C. Kim, S. A. Lee, M. J. Choi, H. Kim, J. W. Yang, J. Lim and H. W. Jang, Hydrothermally obtained type-II heterojunction nanostructures of In_2S_3/TiO_2 for remarkably enhanced photoelectrochemical water splitting, *Appl. Catal., B*, 2021, **295**, 120276.

152 M. G. Lee, J. W. Yang, H. Park, C. W. Moon, D. M. Andoshe, J. Park, C. K. Moon, T. H. Lee, K. S. Choi, W. S. Cheon, J. J. Kim and H. W. Jang, Crystal Facet Engineering of TiO_2 Nanostructures for Enhancing Photoelectrochemical Water Splitting with $BiVO_4$ Nanodots, *Nano-Micro Lett.*, 2022, **14**, 48.

153 S. Pan, R. Li, J. Wang, Q. Zhang, M. Wang, B. Shi, P. Wang, Y. Zhao and X. Zhang, Floating Seawater Splitting Device Based on NiFeCrMo Metal Hydroxide Electrocatalyst and Perovskite/Silicon Tandem Solar Cells, *ACS Nano*, 2023, **17**, 4539–4550.

154 T. L. Kim, M. J. Choi, T. H. Lee, W. Sohn and H. W. Jang, Tailoring of Interfacial Band Offsets by an Atomically Thin Polar Insulating Layer to Enhance the Water-Splitting Performance of Oxide Heterojunction Photoanodes, *Nano Lett.*, 2019, **19**, 5897–5903.

155 M. J. Choi, T. L. Kim, J. K. Kim, T. H. Lee, S. A. Lee, C. Kim, K. Hong, C. W. Bark, K. T. Ko and H. W. Jang, Enhanced oxygen evolution electrocatalysis in strained A-site cation deficient $LaNiO_3$ perovskite thin films, *Nano Lett.*, 2020, **20**, 8040–8045.

156 D. Huang, J. Yu, Z. Zhang, C. Engtrakul, A. Burrell, M. Zhou, H. Luo and R. C. Tenent, Enhancing the Electrocatalysis of $LiNi_{0.5}Co_{0.2}Mn_{0.3}O_2$ by Introducing Lithium Deficiency for Oxygen Evolution Reaction, *ACS Appl. Mater. Interfaces*, 2020, **12**, 10496–10502.

157 M. N. Ates, I. Gunasekara, S. Mukerjee, E. J. Plichta, M. A. Hendrickson and K. M. Abraham, In Situ Formed Layered-Layered Metal Oxide as Bifunctional Catalyst for Li-Air Batteries, *J. Electrochem. Soc.*, 2016, **163**, A2464–A2474.

158 B. Weng, F. Xu, C. Wang, W. Meng, C. R. Crice and Y. Yan, A layered $Na_{1-x}Ni_yFe_{1-y}O_2$ double oxide oxygen evolution reaction electrocatalyst for highly efficient water-splitting, *Energy Environ. Sci.*, 2017, **10**, 121–128.

159 H. Liu, Z. Liu, F. Wang and L. Feng, Efficient catalysis of N doped NiS/NiS_2 heterogeneous structure, *Chem. Eng. J.*, 2020, **397**, 125507.

160 Z. N. Zahran, E. A. Mohamed, Y. Tsubonouchi, M. Ishizaki, T. Togashi, M. Kurihara, K. Saito, T. Yui and M. Yagi, Electrocatalytic water splitting with unprecedentedly low overpotentials by nickel sulfide nanowires stuffed into carbon nitride scabbards, *Energy Environ. Sci.*, 2021, **14**, 5358–5365.

161 C. Zhang, B. Tang, X. Gu and L. Feng, Surface chemical state evaluation of $CoSe_2$ catalysts for the oxygen evolution reaction, *Chem. Commun.*, 2019, **55**, 10928–10931.

162 C. Xia and H. N. Alshareef, Self-templating Scheme for the Synthesis of Nanostructured Transition-Metal Chalcogenide Electrodes for Capacitive Energy Storage, *Chem. Mater.*, 2015, **27**, 4661–4668.

163 M. Wang, Z. Wan, X. Meng, Z. Li, X. Ding, P. Li, C. Li, J. G. Wang and Z. Li, Heterostructured Co/Mo-sulfide catalyst enables unbiased solar water splitting by integration with perovskite solar cells, *Appl. Catal., B*, 2022, **309**, 121272.

164 Y. Kuang, M. J. Kenney, Y. Meng, W. H. Hung, Y. Liu, J. E. Huang, R. Prasanna, P. Li, Y. Li, L. Wang, M. C. Lin, M. D. McGehee, X. Sun and H. Dai, Solar-drivenhighly sustained splitting of seawater into hydrogen and oxygen fuels, *Proc. Natl. Acad. Sci. U. S. A.*, 2019, **116**, 6624–6629.

165 Y. Shi, T. Y. Hsieh, M. A. Hoque, W. Cambarau, S. Narbey, C. Gimbert-Surinãch, E. Palomares, M. Lanza and A. Llobet, High Solar-to-Hydrogen Conversion Efficiency at pH 7 Based on a PV-EC Cell with an Oligomeric Molecular Anode, *ACS Appl. Mater. Interfaces*, 2020, **12**, 55856–55864.

166 H. Liu, X. Peng and X. Liu, Single-Atom Catalysts for the Hydrogen Evolution Reaction, *ChemElectroChem*, 2018, **5**, 2963–2974.

167 K. L. Zhou, Z. Wang, C. B. Han, X. Ke, C. Wang, Y. Jin, Q. Zhang, J. Liu, H. Wang and H. Yan, Platinum single-atom catalyst coupled with transition metal/metal oxide heterostructure for accelerating alkaline hydrogen evolution reaction, *Nat. Commun.*, 2021, **12**, 3783.

168 C. Wei, Y. Sun, G. G. Scherer, A. C. Fisher, M. Sherburne, J. W. Ager and Z. J. Xu, Surface composition dependent ligand effect in tuning the activity of nickel-copper bimetallic electrocatalysts toward hydrogen evolution in alkaline, *J. Am. Chem. Soc.*, 2020, **142**, 7765–7775.

169 Z. Jia, T. Yang, L. Sun, Y. Zhao, W. Li, J. Luan, F. Lyu, L. C. Zhang, J. J. Kruzic, J. J. Kai, J. C. Huang, J. Lu and C. T. Liu, A Novel Multinary Intermetallic as an Active Electrocatalyst for Hydrogen Evolution, *Adv. Mater.*, 2020, **32**, 2000385.

170 H. Park, I. J. Park, M. G. Lee, K. C. Kwon, S. P. Hong, D. H. Kim, S. A. Lee, T. H. Lee, C. Kim, C. W. Moon, D. Y. Son, G. H. Jung, H. S. Yang, J. R. Lee, J. Lee, N. G. Park, S. Y. Kim, J. Y. Kim and H. W. Jang, Water Splitting Exceeding 17% Solar-To-Hydrogen Conversion Efficiency Using Solution-Processed Ni-Based Electrocatalysts and Perovskite/Si Tandem Solar Cell, *ACS Appl. Mater. Interfaces*, 2019, **11**, 33835–33843.

171 Y. Wang, A. Sharma, T. Duong, H. Arandiyan, T. Zhao, D. Zhang, Z. Su, M. Garbrecht, F. J. Beck, S. Karuturi, C. Zhao and K. Catchpole, Direct Solar Hydrogen Generation at 20% Efficiency Using Low-Cost Materials, *Adv. Energy Mater.*, 2021, **11**, 2101053.

172 L. Chen, X. L. Song, J. T. Ren and Z. Y. Yuan, Precisely modifying Co_2P black TiO_2 S-scheme heterojunction by *in situ*, formed P and C dopants for enhanced photocatalytic H_2 production, *Appl. Catal., B*, 2022, **315**, 121546.

173 A. M. Asiri, D. Ren, H. Zhang, S. B. Khan, K. A. Alamry, H. M. Marwani, M. S. J. Khan, W. A. Adeosun, S. M. Zakeeruddin and M. Grätzel, Solar Water Splitting Using Earth-Abundant Electrocatalysts Driven by High-Efficiency Perovskite Solar Cells, *ChemSusChem*, 2022, **15**, 2102471.

174 J. Luo, D. A. Vermaas, D. Bi, A. Hagfeldt, W. A. Smith and M. Grätzel, Bipolar Membrane-Assisted Solar Water Splitting in Optimal pH, *Adv. Energy Mater.*, 2016, **6**, 1600100.

175 H. Roh, H. Jung, H. Choi, J. W. Han, T. Park, S. Kim and K. Yong, Various metal (Fe, Mo, V, Co)-doped Ni2P nanowire arrays as overall water splitting electrocatalysts and their applications in unassisted solar hydrogen production with STH 14%, *Appl. Catal., B*, 2021, **297**, 120434.

176 J. Gao, F. Sahli, C. Liu, D. Ren, X. Guo, J. Werner, Q. Jeangros, S. M. Zakeeruddin, C. Ballif, M. Grätzel and J. Luo, Solar Water Splitting with Perovskite/Silicon Tandem Cell and TiC-Supported Pt Nanocluster Electrocatalyst, *Joule*, 2019, **3**, 2930–2941.

177 S. E. Jun, Y. H. Kim, J. Kim, W. S. Cheon, S. Choi, J. Yang, H. Park, H. Lee, S. H. Park, K. C. Kwon, J. Moon, S. H. Kim and H. W. Jang, Atomically dispersed iridium catalysts on silicon photoanode for efficient photoelectrochemical water splitting, *Nat. Commun.*, 2023, **14**, 609.

178 L. Xie, F. Qu, Z. Liu, X. Ren, S. Hao, R. Ge, G. Du, A. M. Asiri, X. Sun and L. Chen, In situ formation of a 3D core/shell structured Ni_3N@Ni-Bi nanosheet array: An efficient non-noble-metal bifunctional electrocatalyst toward full water splitting under near-neutral conditions, *J. Mater. Chem. A*, 2017, **5**, 7806–7810.

179 T. Wu, M. Z. Sun and B. L. Huang, Non-noble metal-based bifunctional electrocatalysts for hydrogen production, *Rare Met.*, 2022, **41**, 2169–2183.

180 Y. Meng, W. Song, H. Huang, Z. Ren, S. Y. Chen and S. L. Suib, Structure-property relationship of bifunctional MnO_2 nanostructures: Highly efficient, ultra-stable electrochemical water oxidation and oxygen reduction reaction catalysts identified in alkaline media, *J. Am. Chem. Soc.*, 2014, **136**, 11452–11464.

181 Y. Liu, Y. Xing, S. Xu, Y. Lu, S. Sun and D. Jiang, Interfacing Co_3Mo with $CoMoO_x$ for synergistically boosting electrocatalytic hydrogen and oxygen evolution reactions, *Chem. Eng. J.*, 2022, **431**, 133240.

182 W. Zhu, W. Chen, H. Yu, Y. Zeng, F. Ming, H. Liang and Z. Wang, NiCo/NiCo–OH and NiFe/NiFe–OH core shell nanostructures for water splitting electrocatalysis at large currents, *Appl. Catal., B*, 2020, **278**, 119326.

183 K. Hu, M. Wu, S. Hinokuma, T. Ohto, M. Wakisaka, J. I. Fujita and Y. Ito, Boosting electrochemical water splitting: via ternary NiMoCo hybrid nanowire arrays, *J. Mater. Chem. A*, 2019, **7**, 2156–2164.

184 S. Deng, K. Zhang, D. Xie, Y. Zhang, Y. Zhang, Y. Wang, J. Wu, X. Wang, H. J. Fan, X. Xia and J. Tu, High-Index-Faceted Ni_3S_2 Branch Arrays as Bifunctional Electrocatalysts for Efficient Water Splitting, *Nano-Micro Lett.*, 2019, **11**, 12.

185 L. Li, C. Sun, B. Shang, Q. Li, J. Lei, N. Li and F. Pan, Tailoring the facets of Ni_3S_2 as a bifunctional electrocatalyst for high-performance overall water-splitting, *J. Mater. Chem. A*, 2019, **7**, 18003–18011.

186 X. Shi, P. Yang, Y. Cao, C. Dai, W. Ye, L. Zheng, Z. Zhao, J. Wang and H. Zheng, Ultrathin 2D flower-like CoP@C with the active (211) facet for efficient electrocatalytic water splitting, *CrystEngComm*, 2021, **23**, 1777–1784.

187 H. Cao, Y. Xie, H. Wang, F. Xiao, A. Wu, L. Li, Z. Xu, N. Xiong and K. Pan, Flower-like CoP microballs assembled with (002) facet nanowires via precursor route: Efficient electrocatalysts for hydrogen and oxygen evolution, *Electrochim. Acta*, 2018, **259**, 830–840.

188 Z. Yang, F. Shaik, K. Liang, K. Guo, X. Ren and B. Jiang, Self-Supported Phosphorus-Doped Vertically Aligned Graphene Arrays Integrated with FeCoNiP Nanoparticles as Bifunctional Electrocatalysts for Water-Splitting Over a Wide pH Range, *Electron. Mater. Lett.*, 2021, **17**, 87–101.

189 T. Sharifi, C. Larsen, J. Wang, W. L. Kwong, E. Gracia-Espino, G. Mercier, J. Messinger, T. Wågberg and L. Edman, Toward a Low-Cost Artificial Leaf: Driving Carbon-Based and Bifunctional Catalyst Electrodes with Solution-Processed Perovskite Photovoltaics, *Adv. Energy Mater.*, 2016, **6**, 1600738.

190 M. Baek, G. W. Kim, T. Park and K. Yong, NiMoFe and NiMoFeP as Complementary Electrocatalysts for Efficient Overall Water Splitting and Their Application in PV-Electrolysis with STH 12.3%, *Small*, 2019, **15**, 1905501.

191 A. Kumar, D. K. Chaudhary, S. Parvin and S. Bhattacharyya, High performance duckweed-derived carbon support to anchor NiFe electrocatalysts for efficient solar energy driven water splitting, *J. Mater. Chem. A*, 2018, **6**, 18948–18959.

192 J. Ekspong, C. Larsen, J. Stenberg, W. L. Kwong, J. Wang, J. Zhang, E. M. J. Johansson, J. Messinger, L. Edman and T. Wågberg, Solar-Driven Water Splitting at 13.8% Solar-to-Hydrogen Efficiency by an Earth-Abundant Electrolyzer, *ACS Sustainable Chem. Eng.*, 2021, **9**, 14070–14078.

193 L. Ma, W. Zhang, P. Zhao, J. Liang, Y. Hu, G. Zhu, R. Chen, Z. Tie, J. Liu and Z. Jin, Highly efficient overall water splitting driven by all-inorganic perovskite solar cells and promoted by bifunctional bimetallic phosphide nanowire arrays, *J. Mater. Chem. A*, 2018, **6**, 20076–20082.

194 X. Xiao, S. Liu, D. Huang, X. Lv, M. Li, X. Jiang, L. Tao, Z. Yu, Y. Shao, M. Wang and Y. Shen, Highly Efficient Hydrogen Production Using a Reformed Electrolysis System Driven by a Single Perovskite Solar Cell, *ChemSusChem*, 2019, **12**, 434–440.

195 J. Liang, X. Han, Y. Qiu, Q. Fang, B. Zhang, W. Wang, J. Zhang, P. M. Ajayan and J. Lou, A Low-Cost and High-Efficiency Integrated Device toward Solar-Driven Water Splitting, *ACS Nano*, 2020, **14**, 5426–5434.

196 C. Hu, X. Chen, Q. Dai, M. Wang, L. Qu and L. Dai, Earth-abundant carbon catalysts for renewable generation of clean energy from sunlight and water, *Nano Energy*, 2017, **41**, 367–376.

197 M. Schreier, L. Curvat, F. Giordano, L. Steier, A. Abate, S. M. Zakeeruddin, J. Luo, M. T. Mayer and M. Grätzel, Efficient photosynthesis of carbon monoxide from CO_2 using perovskite photovoltaics, *Nat. Commun.*, 2015, **6**, 8326.

198 S. Esiner, J. Wang and R. A. J. Janssen, Light-Driven Electrochemical Carbon Dioxide Reduction to Carbon Monoxide and Methane Using Perovskite Photovoltaics, *Cell Rep. Phys. Sci.*, 2020, **1**, 100058.

199 W. Zhang, Y. Xia, S. Chen, Y. Hu, S. Yang, Z. Tie and Z. Jin, Single-Atom Metal Anchored Zr6-Cluster-Porphyrin Framework Hollow Nanocapsules with Ultrahigh Active-Center Density for Electrocatalytic CO_2 Reduction, *Nano Lett.*, 2022, **22**, 3340–3348.

200 T. N. Huan, D. A. D. Corte, S. Lamaison, D. Karapinar, L. Lutz, N. Menguy, M. Foldyna, S. H. Turren-Cruz, A. Hagfeldt, F. Bella, M. Fontecave and V. Mougel, Low-cost high-efficiency system for solar-driven conversion of CO_2 to hydrocarbons, *Proc. Natl. Acad. Sci. U. S. A.*, 2019, **116**, 9735–9740.